Journal of Sailing Technology 2026, volume 11, issue 1, pp. 137 – 164.
The Society of Naval Architects and Marine Engineers.

Fully Automated Wind Tunnel Experiments for Performance Prediction of a Double Rotor Sail

Kai Hillers
Fraunhofer WG Sustainable Maritime Mobility, Emden/Leer University of Applied Sciences, Germany, kai.hillers@hs-emden-leer.de.

Arne Daniel
Fraunhofer WG Sustainable Maritime Mobility, Emden/Leer University of Applied Sciences, Germany.

Jann Strybny
Fraunhofer WG Sustainable Maritime Mobility, Emden/Leer University of Applied Sciences, Germany.

Manuscript received December 12, 2025; revision received March 24, 2026; accepted April 7, 2026.

Abstract. Flettner rotors are increasingly explored as a sustainable hybrid propulsion technology in maritime applications, yet predictive tools for multi-rotor installations remain limited, particularly when rotors are independently controlled. This study presents an experimental investigation of a double Flettner rotor system, employing a fully automated wind tunnel setup with independent spin ratios. Two identical rotors ($L/D = 6$, $D_e/D = 2$, $D = 0.09\,\mathrm{m}$) were tested over $\lambda_1, \lambda_2 \in [0,5]$, inflow angles $\varphi \in [0°, 90°]$, spacings $S/D \in \{2.2, 3, 4\}$, and three free stream velocities ($Re \approx 5 \times 10^4 - 1 \times 10^5$). The sense of rotation was used only to cover angles of $\varphi > 90°$. The fully automated setup acquired 10164 configurations, each repeated three times. We map projected thrust and side force coefficients (c_x, c_y) across ($\lambda_1, \lambda_2, \varphi, S/D$) and distill design-relevant trends. Within the tested ranges: (i) increasing spacing from raises c_x for all operative points; (ii) optimal operating points are frequently asymmetric, with the windward rotor commanded at up to ~50% lower spin ratio than the leeward; (iii) the downstream rotor in the wake can exhibit up to ~11% higher lift than the upstream rotor at comparable operating points; (iv) a lateral deck alignment achieves ~10% higher peak c_x compared to a longitudinal alignment at $S/D = 4$ when each is operated at its optimal (λ_1, λ_2) across φ. We present compact c_x-c_y polars and lookup tables over the measured grid to enable simple performance prediction and control scheduling.

Keywords: flettner rotors; double rotor system; Magnus effect; performance prediction; sailing polar; wake effect

NOMENCLATURE

A	Area [m²]
b_i	Components of solution vector [-]
$\mathbf{c}$	Relative corrective balance torque [-]
c_D	Aerodynamic drag force coefficient [-]
c_L	Aerodynamic lift force coefficient [-]
c_x	Aerodynamic force coefficient in the x-direction [-]
c_y	Aerodynamic force coefficient in the y-direction [-]
C_μ	Model constant applied in turbulence modelling [-]
D	Diameter of the rotor [m]
d'	Drag vector component [-]

D_e Diameter of the rotor's endplates [m]
D_e/D Non-dimensional rotor's endplate ratio [-]
F_x Aerodynamic force in the x-direction [N]
F_y Aerodynamic force in the y-direction [N]
$\mathbf{h}$ Relative influence coefficient [-]
I Turbulence Intensity [-]
k Turbulent kinetic Energy [m² s^{-2}]
k_{cov} Coverage factor [-]
L Length of the rotor [m]
l' Lift vector component [-]
L_C Characteristic Length [m]
L_t Turbulent length scale [m]
r_i Trial weight for balancing run [kg]
Re Reynolds number [-]
Re_{rot} Reynolds number of rotating cylinder [-]
S Distance between rotors [m]
S/D Non-dimensional distance ratio between rotors [-]
u_∞ Free stream wind velocity [m s^{-1}]
$\bar{u}_\infty$ Mean value of free stream wind velocity [m s^{-1}]
u_w Near wall wind velocity [m s^{-1}]

α Rotational direction [-]
γ_i Angle of trial weight [°]
ε Turbulent dissipation rate [m² s^{-3}]
λ Speed ratio of rotor [-]
λ_1 Speed ratio of rotor 1 [-]
λ_2 Speed ratio of rotor 2 [-]
ν Kinematic viscosity [m² s^{-1}]
ν_T Turbulent viscosity [m² s^{-1}]
ξ Propagated error [%]
ρ Fluid density [kg m^{-3}]
σ Standard deviation [-]
τ Torque [Nm]
φ Angle of attack [°]
ω Rotational Speed of rotor [rad s^{-1}]

CFD Computational Fluid Dynamics

1. INTRODUCTION

The Flettner rotor and its working principle, the Magnus effect, have been investigated for more than 100 years. First publications by Reid (1924) explored the geometry of the Magnus effect by comparing a circular cylinder to a cross cylinder and a compound strut. Thom (1934) analysed the cylinder parameters like diameter, length, rounded ends and its roughness. Prandtl (1925) found that flow separated early at the ends of the rotor and greatly increased its performance by adding endplates to the rotor. Additionally, he assessed the Magnus effect mathematically by superposing two potential flow fields, which led him to defining the physical maximum performance limit of a rotating cylinder, the Prandtl limit. Since then, there have been multiple publications trying to assess the performance of Flettner rotors through wind tunnel experiments, computational fluid dynamics or measurements on Flettner rotors in operation on a vessel. For a long time, this topic was not paid attention, since combustion engines have been more profitable for commercial shipping. With the emerging transition to more sustainable and green shipping, this topic has picked up traction again. Points of interest have shifted a bit, because technology allows for more exact measurements, better wind tunnels and more complex experiments. Bordogna, et al. (2019) tested a single Flettner rotor

at super critical Reynolds numbers and found that lift and drag of a Flettner rotor have a Reynolds number dependency. Similar findings were documented by Ma, et al. (2022) with more emphasis on studying the wake and turbulence of the rotors flow. Chen, et al. (2023) published an in-depth parametric study of single Flettner rotor geometry and a double Flettner rotor system interference. The double Flettner rotor system's performance was assessed at different inflow-angles, rotational rates and spacings between rotors. For that purpose, Chen let both rotors rotate at the same rotational speed, rotated the double rotor system in seven angles from 0° to 360° and tested two different spacings $S/D = 5$ and $S/D = 10$. Similar to that, Bordogna, et al. (2020) investigated the aerodynamic interaction of two Flettner rotors at speed ratios of $\lambda = 1$, $\lambda = 1.5$ and $\lambda = 2$ and rotor spacings of $S/D = 3$, $S/D = 7.5$ and $S/D = 15$.

Despite renewed interest in wind-assisted ship propulsion, predictive tools for double rotor performance remain limited. The existing studies by Bordogna, et al. (2020) and Chen, et al. (2023) assess two rotors at equal or restricted speed ratios and inflow angles, providing limited guidance for independent spin control and installation choices. Designers therefore cannot reliably predict, across the operating envelope, how two interacting rotors combine to produce net thrust-force when rotor spacing S/D, inflow angle φ and speed ratios λ_1, λ_2 are varied independently.

This study presents wind tunnel experiments with a fully automated experimental setup for a double Flettner rotor system of two identical rotors. Their geometry is defined by an aspect ratio of $L/D = 6$, an endplate ratio of $D_e/D = 2$ and a diameter of $D = 0.09\ \mathrm{m}$. The experimental parameters that are being systematically varied are the rotational speed of both rotors independently, the inflow-angle, the distance between rotors and the wind speed. The tested rotational speeds range from $\lambda = 0$ to $\lambda = 5$ in steps of $\lambda = 0.5$, the inflow-angles range from 0° to 90° in 15° steps, the distances tested are $S/D = \{2.2, 3, 4\}$ and the Reynolds numbers range from $Re = 50000$ to $Re = 100000$ with three different wind speeds. This results in 7623 parameter combinations that are all tested and set automatically during wind tunnel operation. Additionally, the rotational direction α is varied between clockwise and counter-clockwise, but only for the tests at lowest wind speed, resulting in another 2541 parameter combinations. The direction of rotation is not examined as an independent parameter, but was only used to extend the angle range from 0-90° to 90-180°. In total, one measurement series consists of 10164 single measurements, closing the gap of having any arbitrary combination of speed ratios tested at all relevant inflow conditions. Our research question is: How do λ_1, λ_2, S/D and φ jointly govern aerodynamic performance, measured as thrust-coefficient, in a double rotor system? With the systemic map of double rotor performance, we want to test if asymmetric spin pairs ($\lambda_1 \neq \lambda_2$) exist. Another insight we want to provide is the rotor placement, whether a longitudinal or lateral arrangement of Flettner rotors on a vessel gives higher thrust. The data provides insight into rotor interactions and performance at all possible operation conditions as functions of λ_1, λ_2, S/D, φ. Results show that it is not optimal to always run rotors at maximum speed and neither is it necessary to have them run at the same speed ratio for maximum performance. For maximum c_x-performance speed ratios of the windward rotor are up to 50% lower than the leeward rotors speed ratio. The data also shows that for all tested distances an installation along the lateral axis of a vessel achieves roughly 10% higher thrust-coefficient values than installing the rotors along the longitudinal axis for their respective maximum thrust-coefficient values at spacing of $S/D = 4$.

The measurement series were repeated three times for statistical certainty. With this test matrix, the sailing system's performance is tested in wind scenarios from 0° to 180°, giving an overview of its aerodynamic performance in the form of a polar diagram of thrust and side force coefficients.

This document is structured as follows. First, the experimental setup is detailed along with the geometry data, parameter spaces, uncertainties, calibration, and data acquisition. Next, the theoretical knowledge is explained, introducing all relevant equations used to evaluate the data, followed by a discussion about Reynolds number effects on Flettner rotors. Then, the data evaluation is presented and a data reduction strategy is outlined. After that, the results are discussed and placed in the context of historical data. Finally, the paper closes with a summary of the main findings and a simple working example showing how the data can be used for a performance prediction.

2. EXPERIMENTAL SETUP

The measurements take place in the wind tunnel of the Maritime Laboratory of the Emden/Leer University of Applied Sciences. It is a WK 880050-E wind tunnel by Westenberg Engineering, which is an Eiffel-style wind tunnel that generates flow by suctioning the air with the turbine rotor at downstream position. The closed measuring section of this wind tunnel is of 1.1 m length, 2 m wide, 2.5 m in height and has an inlet nozzle of 0.8 m diameter that feeds the test section and an outlet collector of 1.0 m diameter. Together with the model rotor dimensions of 0.54 m height and 0.09 m diameter, the geometric blockage, defined as the projected area of the double rotor system divided by the tunnel cross area, ranges from 1% to 2% depending on the angle of attack. The wind tunnel generates uniform flow with low angularity and wind speeds of up to 50 m/s with a turbulence intensity of 0.5% to 0.8% at 20 m/s wind speed. With its flow calculation system, the wind speed is set with an uncertainty of 0.5% of target velocity, but minimum 0.01 m/s. The flow calculation system uses a pitot tube for controlling the wind speed. Air density ρ was calculated from barometric pressure, temperature, and relative humidity measured in the test section (barometer 800-1100 mbar, accuracy ±0.5%; T-RH probe -40 to 60 °C and 2-98% RH, accuracies ±0.2 °C and ±2% RH). These inputs were used to update ρ in real time, giving a relative density uncertainty on the order of 0.5%. A timeseries of the tested wind speeds and their respective 30 seconds segmented turbulence intensities can be found in Fig. 1. The wind speeds in these timeseries have been measured with a Thies Clima ultrasonic 3D anemometer at 100 Hz with an uncertainty of ± (0,1 m/s + 1 %) rms.

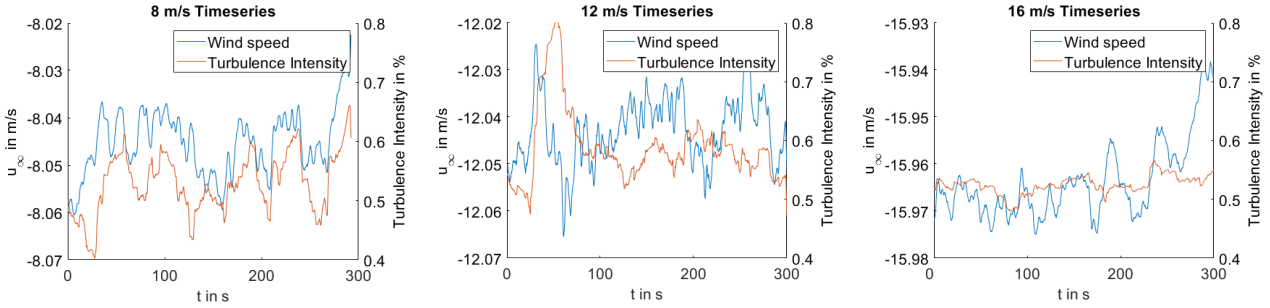

(a) $u_\infty = 8\ \mathrm{m/s}$ **(b)** $u_\infty = 12\ \mathrm{m/s}$ **(c)** $u_\infty = 16\ \mathrm{m/s}$

Figure 1. Timeseries of tested wind speeds.

Inside the measuring section, the experiment was set up in the centre of the core flow. The construction is designed in a modular way, so that it is not restricted to Flettner rotors but allows examination of any kind of two-mast sail system. The experimental setup is fully automated and allows setting the parameters during wind tunnel operation. For that reason, a hollow shaft actuator with a ring gear connected to a stepper motor is used to implement the angle sweep. Its combined angle-setting uncertainty derived from manufacturer specification is given as ±0.038°. The distance adjustment was made possible by using a linear axis driven by a stepper motor. The system has repeatability of ±0.1 mm and a belt strain of 0.21%, resulting in a maximum uncertainty of ±0.0098 S/D or ±0.88 mm in a worst-case scenario. Angle sweep and rotor spacing have been validated using analogue methods. Milling spindles were used to drive the rotors, as these have a high load capacity and usually come with a cooling system, which was a necessary requirement for avoiding overheating motors in long-time measurements. The spindles are controlled by a variable frequency drive with a combined frequency uncertainty of ±0.047 Hz or ±0.031% at maximum frequency of 150 Hz used during the measurement series. The variable frequency drives speed commands were validated against the optical tachometer Testo 460 with an accuracy of ±0.02% of reading. All tested frequencies have been validated and showed agreements within given accuracy.

Figure 2 shows the experimental setup with its two Flettner rotors, an aerodynamic cover of automation components and the measurement section of the wind tunnel.

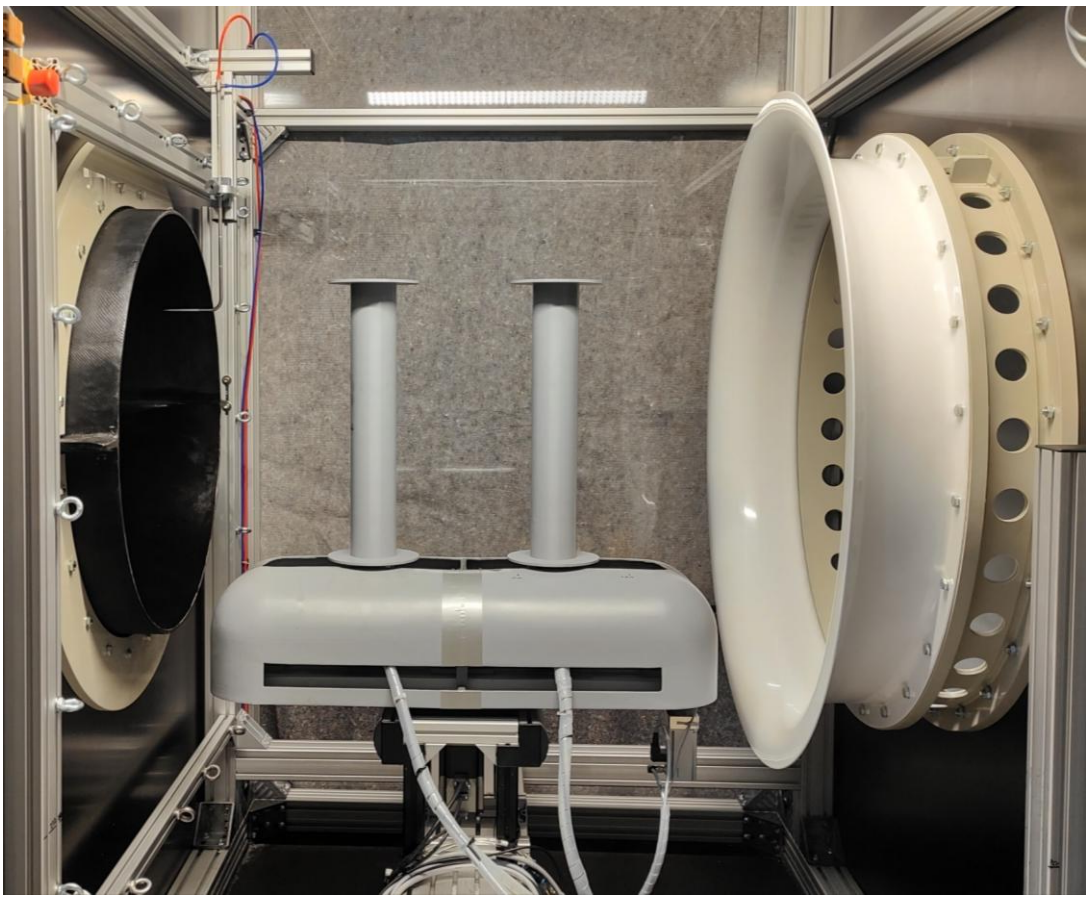

Figure 2. Fully automated experimental setup in the wind tunnel.

The Flettner rotors are based on the design of the EcoFlettner 18x3 rotor and were 3D-Printed and assembled from two parts. After assembly and testing they are sanded for a smooth surface. The milling spindles driving the rotors are placed inside the rotors and use an ER11 tool holder for holding the shaft. On top of the milling spindle an aluminium tube is placed with a tight fitting. This aluminium tube holds a bearing for the shaft and the shaft is fixed at the top of the rotor with a form locking and a screw. The aluminium tube also serves as seat for the upper bearing inside of the rotor. The lower rotor bearing is placed on the casing of the milling spindle. The milling spindle is held by a mechanical clamp that is connected to the 6-axis force sensor through a base plate. Figure 3 shows a cross-sectional view of the detailed construction. Both rotors have their own sensor. The sensor used is a K6D40 by ME Meßsysteme with a nominal force of 500 N in x- and y-axis and 2 kN in z-axis. Its measurement uncertainty is specified as ±0.1% of its nominal value and its crosstalk is corrected with the proper matrix supplied by the manufacturer. The force sensors x-axis is aligned with the longitudinal axis of the setup, as seen in Fig. 4. In addition, we verified the sensor scale factors by deadweight checks: calibrated 2 kg masses were applied along the axes. The measured forces agreed within the manufacturer's ±0.1% specification. In an effort to reduce the systems interference with the force measurements, the force sensors and the rotors support were shielded from the wind. An aerodynamic tare test without rotors showed forces within the measurement uncertainty across the tested angles and speeds. Therefore, support-induced aerodynamic loading was deemed negligible. The nomenclature of rotors is rotor 2 for the rotor hit by the wind first and rotor 1 for the rotor in the back. The whole construction is connected to the linear axis with a connection plate.

The blockage has been accounted for according to the blockage and wake correction of Glauert (1933), where the whole setup is assumed as an ellipse with the fineness ratio of the respective rotor spacing.

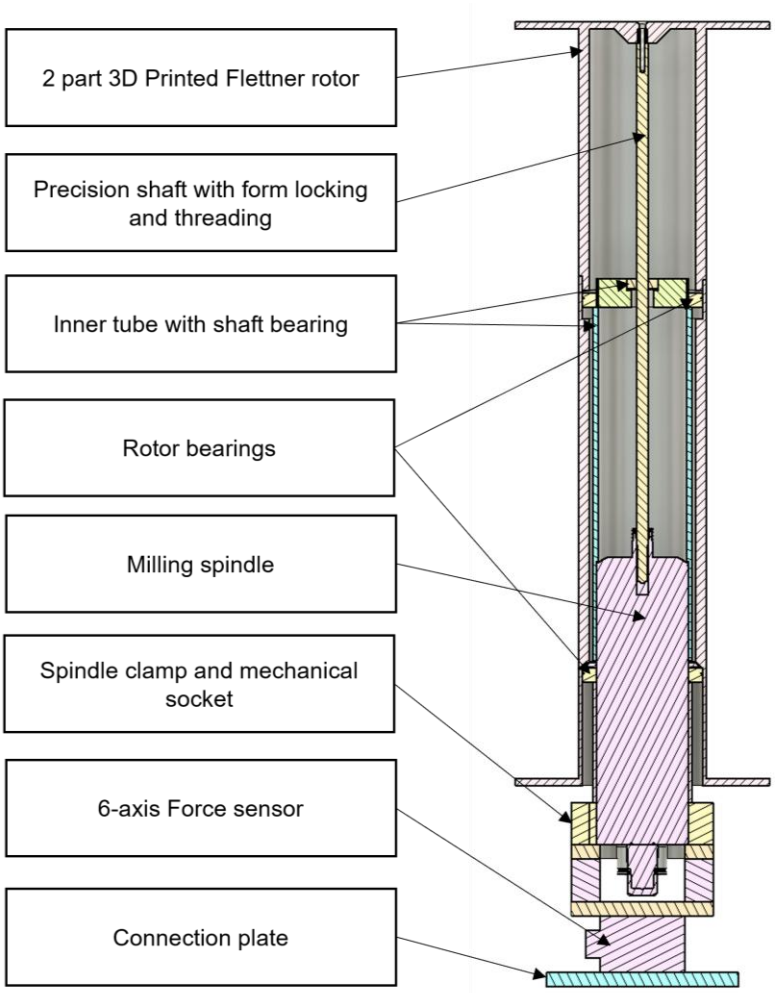

Figure 3. Flettner rotor construction in the wind tunnel.

2.1 Balancing of Rotors

The 3D printed Flettner rotors always came with a slight rotational imbalance which had to be balanced for the systems longevity. For that purpose, the methodology of Foiles and Allaire (2006) was used in a slightly modified way. Since the Flettner rotor construction only includes the 6-axis force sensor, the displacement by vibrations could not be evaluated. Instead, the torque at the bottom of the rotor was used to have a relative measure of the vibrations. This had the consequence that the corrective balance weight could not be calculated, but had to be found experimentally by additional measurements.

The methodology of Foiles and Allaire (2006) requires four measurements of which one is without additional weight and three measurements with a defined weight placed at 0°, 135° and 270°. The weight used for the first run was 1 gram of kneaded seal, which was subsequently varied in following runs. As already mentioned, the measured variable is the torque at the root of the rotor. The amplitude of the torque measurements is then used to solve the system of equations seen in Eq. 1.

$$\begin{bmatrix} 2\hat{\tau}r_1\cos(\gamma_1) & -2\hat{\tau}r_1\sin(\gamma_1) & r_1^2 \\ 2\hat{\tau}r_2\cos(\gamma_2) & -2\hat{\tau}r_2\sin(\gamma_2) & r_2^2 \\ 2\hat{\tau}r_3\cos(\gamma_3) & -2\hat{\tau}r_3\sin(\gamma_3) & r_3^3 \end{bmatrix} \begin{pmatrix} b_1 \\ b_2 \\ b_3 \end{pmatrix} = \begin{pmatrix} \hat{\tau}_1^2 - \hat{\tau}^2 \\ \hat{\tau}_2^2 - \hat{\tau}^2 \\ \hat{\tau}_3^2 - \hat{\tau}^2 \end{pmatrix} \quad (1)$$

Where $\hat{\tau}$ is the amplitude of the torque, r is the weight used, γ is the angle at which the weight is placed and (b_1, b_2, b_3) is the solution vector. Additionally, Foiles and Allaire (2006) give a relative influence coefficient seen in Eq. 2.

$$\mathbf{h} = b_1 + \mathrm{i}b_2 \tag{2}$$

This relative influence coefficient $\mathbf{h}$ describes the effect of the weight relative to the original vibration. The coefficient can then be used to calculate the angle at which the corrective weight has to be placed for balancing according to Eq. 3.

$$\mathbf{c} = \frac{-\hat{\tau}}{\mathbf{h}} \tag{3}$$

The complex number $\mathbf{c}$ gives the angle at which the corrective weight has to be placed. Its magnitude does not describe the amount of weight but rather the amount of torque that has to be generated by the corrective weight. That is why, additional measurements with small variations of the corrective weight were made to find the weight under which the vibrations were at the lowest.

The following example explains how to calculate the weight position using a full balancing run consisting of four measurements seen in Tab. 1.

Table 1. Exemplary balancing run.

Run	Trial weight phase γ_i	Torque amplitude $\hat{\tau}_i$ in Nm
1	Initial run	2.4976
2	0°	1.3820
3	135°	3.0705
4	270°	4.1752

The system of equations from Eq. 1 then becomes:

$$\begin{bmatrix} 2 \cdot 2.4976 \cdot 1 \cdot \cos(0°) & -2 \cdot 2.4976 \cdot 1 \cdot \sin(0°) & 1^2 \\ 2 \cdot 2.4976 \cdot 1 \cdot \cos(135°) & -2 \cdot 2.4976 \cdot 1 \cdot \sin(135°) & 1^2 \\ 2 \cdot 2.4976 \cdot 1 \cdot \cos(270°) & -2 \cdot 2.4976 \cdot 1 \cdot \sin(270°) & 1^2 \end{bmatrix} \begin{pmatrix} b_1 \\ b_2 \\ b_3 \end{pmatrix} = \begin{pmatrix} 1.3820^2 - 2.4976^2 \\ 3.0705^2 - 2.4976^2 \\ 4.1752^2 - 2.4976^2 \end{pmatrix}$$

Which, when solved, gives

$$\begin{pmatrix} b_1 \\ b_2 \\ b_3 \end{pmatrix} = \begin{pmatrix} -1.5335 \\ 1.5738 \\ 3.3322 \end{pmatrix}$$

From this, the relative influence coefficient is easily constructed with Eq. 2

$$\mathbf{h} = -1.5335 + \mathrm{i}1.5738$$

And the relative corrective torque and corrective weight angle with Eq. 3

$$\mathbf{c} = \frac{-2.4976}{-1.5335 + i1.5738} = 0.7932 + i0.8141 = (1.1366, -134.25°)$$

3. THEORETICAL KNOWLEDGE

From the measured forces a dimensionless force coefficient is calculated according to Eq. 4.

$$c_i = \frac{F_i}{0.5\rho A u_\infty^2} \tag{4}$$

Indices i of c and F indicate the reference system of this value, e.g. F_x is the force acting in x-direction. Since there are two reference frames, the one of the sensor axis directions and the one of the free stream direction, possible indices i are x, y, z and l, d, c (lift, drag, cross). The area A in Eq. 4 is the projected area of the double Flettner rotor system. The density ρ is the density of the wind tunnels fluid and u_∞ is the wind tunnel free stream velocity. The sensors are fixed and rotated in fixed orientation with the axis in line of the double Flettner rotor system, thus a coordinate transformation is needed for every angle of attack to determine the lift l' and drag d' as in Eq. 5. Figure 4 gives a visualization of the different reference frames in the wind tunnel.

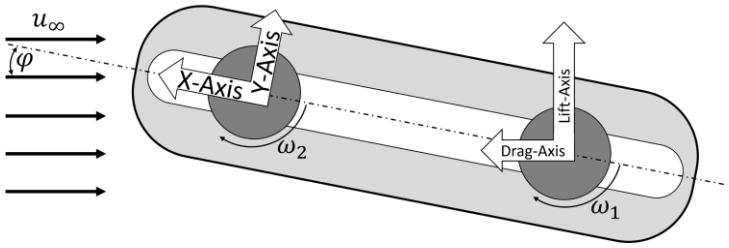

Figure 4. Schematic top view of the wind tunnels reference frames.

$$F_i = \begin{pmatrix} d' \\ l' \end{pmatrix} = \begin{pmatrix} \cos(\varphi') & -\sin(\varphi') \\ \sin(\varphi') & \cos(\varphi') \end{pmatrix} \begin{pmatrix} x \\ y \end{pmatrix} \tag{5}$$

The forces can then be described as functions of the six parameters that are being varied in the wind tunnel, as in Eq. 6.

$$F_i = f(\omega_1, \omega_2, \varphi, S, u_\infty, \alpha) \tag{6}$$

Since the forces acting on the rotor through fluid motion are impacted by rotational speed ω and free stream wind velocity u_∞, it is common practice to combine these parameters into the so-called speed ratio λ, as can be seen in Eq. 7. The speed ratio describes the ratio circumferential velocity $\omega D/2$ to wind velocity u_∞.

$$\lambda = \frac{\omega D}{2u_\infty} \tag{7}$$

Additionally, the distance of rotors can be made dimensionless by dividing the distance of the rotors by their diameter. This simplifies Eq. 6 to

$$F_i = f(\lambda_1, \lambda_2, \varphi, S/D, u_\infty, \alpha) \tag{8}$$

By using the symmetry of the problem and a coordinate transformation equivalent to Eq. 5, the results can be transformed by 90° to assess a system with rotors aligned along the lateral axis.

The turbulence intensity I is defined as the standard deviation σ of a wind speed timeseries divided by the wind speeds mean value $\bar{u}_\infty$ of respective timeseries, as seen in Eq. 9.

$$I = \frac{\sigma}{\bar{u}_\infty} \tag{9}$$

Another turbulent metric is the turbulent kinetic energy k, which is defined as the sum of the variances σ_i^2 of the fluctuating velocity components. A commonly used approximation under the assumption of isotropy of the flow uses the free stream wind speed and turbulence intensity, as seen in Eq. 10.

$$k = \frac{1}{2}\left(\sigma_x^2 + \sigma_y^2 + \sigma_z^2\right) \approx \frac{3}{2}(u_\infty I)^2 \tag{10}$$

From the $k-\varepsilon$ turbulence closure model more relevant equations arise. The specific turbulent dissipation rate ε describes how fluctuations at the smallest turbulent length scales decay. Its calculation can be seen in Eq. 11,

$$\varepsilon = C_\mu^{3/4} \frac{k^{3/2}}{L_t}, \tag{11}$$

where C_μ is a model constant ($C_\mu \approx 0.09$) and L_t is the turbulent length scale. The turbulent length scale describes the size of eddies in a turbulent flow.

The $k-\varepsilon$ turbulence model uses the turbulent viscosity, as seen in Eq. 12, to model increased momentum transfer and energy dissipation caused by eddy motions, which simulates enhanced mixing.

$$\nu_t = \frac{C_\mu}{\varepsilon} k^2 \tag{12}$$

3.1 Reynolds Number of Flettner Rotors

The tested Reynolds numbers in this study are $Re \approx 5 \times 10^4 - 1 \times 10^5$ respective for $u_\infty = \{8, 12, 16\}\ \mathrm{m/s}$. Historically, the calculation of a Flettner rotors Reynolds number was identical to the calculation of a static cylinder. The Reynolds number reflects the ratio of inertia-forces to viscous-forces and plays a huge role in downscaled aerodynamic model experiments. When the Reynolds number stays the same between nature- and model-scale, the flow field is similar. The Reynolds number can be calculated using Eq. 13,

$$Re = \frac{u_\infty L_C}{\nu}, \tag{13}$$

where u_∞ is the freestream velocity, L_C is the characteristic length of the geometry in the flow and ν is the kinematic viscosity. Another crucial property of the Reynolds number is the correlation between the Reynolds number and the transition to turbulent flows. This threshold is called the critical Reynolds number and it changes with respect to the geometry and form. For stationary cylinders it is known that the critical Reynolds number is at $Re \approx 2 \times 10^5$ (Achenbach, 1968). At this flow condition the drag coefficient of the cylinder decreases drastically from $c_D \approx 1.2$ to $c_D \approx 0.3$ which was found to be caused by the flow forming a separation bubble, followed by a turbulent reattachment. Past this Reynolds number regime, the flow turns into a supercritical flow, where an immediate transition from the laminar to the turbulent boundary layer is observed at a critical distance from the stagnation point. In the supercritical flow, the drag coefficient increases a little, but does not go back to its value in subcritical flow. As one can see from this, the Reynolds number and the flow transitions are related to the flow in the near field of the geometry, the boundary layer. Now, imposing a rotation on the cylinder definitely has an effect on the cylinders boundary layer and changes the flow around it. This can easily be proven if one compares the streamlines derived from potential

theory around a stationary and a rotating cylinder, as seen in Fig. 5. It is obvious, that the flow does change when imposing a rotation on the cylinder, so it is implausible to use the Reynolds number as seen in Eq. 13 to quantify the flow conditions around a rotating cylinder. The change in the flow field is induced by viscous momentum transfer from the cylinder's circumferential velocity. Using the boundary layer theory proposed by Prandtl (1904) and Karman (1931) one could argue, that the free stream fluid velocity and the circumferential velocity of the rotor are adding up at the point where both are aligned, resulting in the near wall velocity described in Eq. 14.

$$u_w = u_\infty(1 + \lambda) \tag{14}$$

The resulting Reynolds number calculated with u_w instead of u_∞ would be different for each rotational speed. It would become the multiple of the stationary cylinder's Reynolds number depending on the speed ratio, as seen in Eq. 15.

$$Re_{rot} = \frac{u_\infty L_C}{\nu}(1 + \lambda) \tag{15}$$

This would imply, that the flow past a rotating cylinder is always at least critical, as long it is in the critical regime of a stationary cylinder. Coherently, the drag coefficient decreases within the critical Reynolds number regime and increases in the supercritical regime until its threshold, which is known as the characteristic property drag coefficient curve of Flettner rotors. Meaning that beyond a certain speed ratio, the flow around the rotor no longer changes significantly, as the points of flow attachment and detachment collapse into a single location. Consequently, the flow becomes largely independent of the Reynolds number, and the streamline patterns appear nearly identical across different Reynolds numbers. This was also found by Karabelas, et al. (2012), studying rotating cylinders at supercritical Reynolds numbers numerically with computational fluid dynamics (CFD).

When acknowledging the circumferential velocity of the rotor in the Reynolds number, the tested Reynolds numbers become $Re_{rot} \approx 3 \times 10^5 - 6 \times 10^5$ for $\lambda = 5$ and stay the same as stated earlier for $\lambda = 0$.

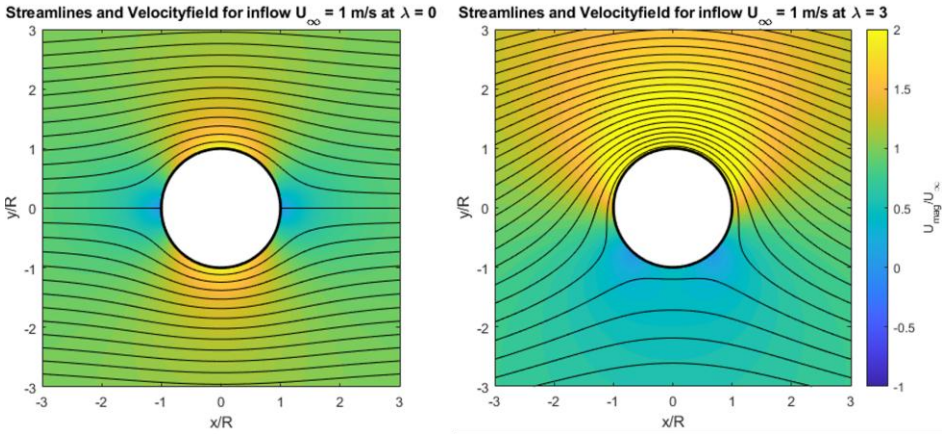

Figure 5. Comparison between potential flow field around cylinder at $\lambda = 0$ and $\lambda = 3$ at $u_\infty = 1\ \mathrm{m/s}$.

4. DATA EVALUATION

In the previous section, the evaluation of a single state from the parameter set $\{\lambda_1, \lambda_2, \varphi, S/D, u_\infty\}$ has been discussed. Now, the challenge is to find combinations of elements in this set that result in insightful visualizations. It is impossible to show the entirety of the data in a single plot since we can only visualize the function values in dependency of three parameters. Two parameters will then span an area between the abscissa- and ordinate-axis, while the plotted function value will be on the applicate-axis. This creates a curved surface in a 3D space. To add another dimension of

information, one can add a colour table to the plot. Figure 6 shows the function $c_x(\lambda_1, \lambda_2, \varphi)$ with each surface representing one of the investigated angles of attack. Each plot contains the $c_x(\lambda_1, \lambda_2, \varphi)$-data for a set distance and wind speed, so that the nine plots seen in Figs. 6a-6i visualize the whole data of $c_x(\lambda_1, \lambda_2, \varphi, S/D, u_\infty)$. Although function values such as the thrust coefficient are measured individually at both rotors, only the combined total value of both rotors is relevant for the evaluation.

4.1 Thrust Coefficient

The thrust coefficient c_x is calculated according to Eq. 4 with the measured force in x-direction F_x, the measured density ρ, the projected area of the double rotor system A and the free stream wind speed u_∞. With the known uncertainties of these quantities, the propagated error of force coefficients is $\xi_c = 1.94\%$ under the assumption of rectangular distribution and a coverage factor of $k_{cov} = \sqrt{3}$. The propagated error of the speed ratio is $\xi_\lambda = 0.5\%$ under the same assumptions.

From Fig. 6a to Fig. 6i the general patterns of the emerging thrust coefficient surfaces remain relatively consistent across different wind speeds. Along the diagonal axis where $\lambda_1 = \lambda_2$, the surfaces corresponding to higher angles of attack exhibit a degree of symmetry in the resulting thrust coefficients. Configurations where rotors separation is $S/D = 2.2$ yield significantly lower thrust in total. Notably, at lower angles of attack the maximum thrust does not occur when both rotors operate at their maximum speed ratios. This can be observed if looking closely at Fig. 6a and Fig. 6b, where the maximum is located at $\lambda_1 = 5$, $\lambda_2 = 2.5$ for $S/D = 2.2$ and $\lambda_1 = 5$, $\lambda_2 = 4$ for $S/D = 3$. This suggests that at the spacing of $S/D = 4$ the mutual rotor interference of rotor 2 and rotor 1 is the lowest for all tested spacings. The dark blue surface, representing an angle of attack of $\varphi = 0°$, shows that rotor 1 generates almost no thrust when it is placed directly downstream of the stationary rotor 2. This aligns with expectations, as rotor 1 lies fully within the wake of the stationary rotor 2. Conversely, when rotor 1 is stationery and rotor 2 is rotating, a measurable thrust is generated by rotor 2. Furthermore, for angles of attack $\varphi \geq 45°$, rotor 1 generally produces more thrust than rotor 2. This can be attributed to increased turbulence in the inflow on rotor 2 due to the wake from rotor 1. At $\varphi = 90°$, the thrust slightly decreases, which may be explained by both rotors being aligned perpendicular to the flow direction, thus experiencing similar inflow conditions. These observations suggest that turbulence intensity should be considered as an additional parameter in future analysis.

Across the range of speed ratios and angles of attack illustrated in Fig. 6b to Fig. 6c, it becomes evident that the optimal thrust conditions shift progressively with increasing rotor speeds. Specifically, for λ_1 and λ_2 values up to approximately 2, the surface corresponding to $\varphi = 90°$ produces the highest thrust. As the speed ratios increase to around $\lambda_1 = 3$, $\lambda_2 = 3$, the maximum thrust shifts to an angle of attack of $\varphi = 75°$. Beyond this region, a narrow beltway can be identified at $\lambda_1 = 4$, $\lambda_2 = 4$, where $\varphi = 60°$ yields the highest thrust. At higher rotational speeds, the increase in thrust becomes less pronounced, forming a plateau. This plateau corresponds to $\varphi = 45°$, indicating a saturation point beyond which further increases in rotational speed or angle of attack do not result in significant thrust gains.

Figures 6d through 6i demonstrate that the resulting thrust coefficients remain largely unchanged with increasing wind speed, indicating that the system's aerodynamic performance is Reynolds number independent within the investigated range of speed ratios. This behaviour suggests that the flow regime remains fully turbulent and geometrically similar across the tested Reynolds numbers, which is characteristic of large-scale rotor systems operating at moderate to high speeds. Consequently, any changes in dynamic pressure due to higher wind speeds are offset by proportional increases in rotor speed, preserving the thrust coefficient behaviour. Based on this observation, the subsequent analysis will focus exclusively on the dataset corresponding to a freestream velocity of $u_\infty = 8\,\mathrm{m/s}$, as it is representative of the entire Reynolds number range considered.

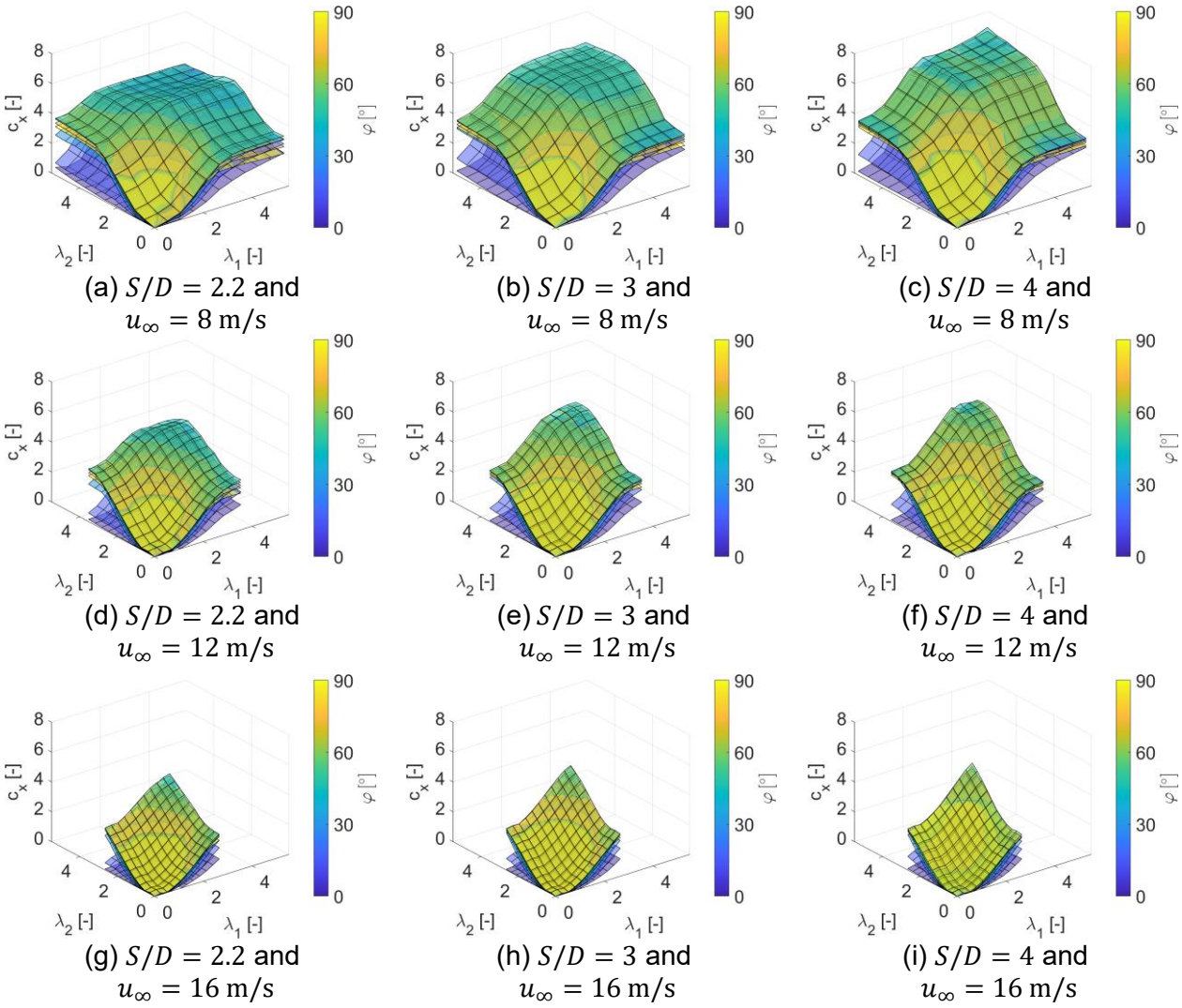

(a) $S/D = 2.2$ and $u_\infty = 8\ \mathrm{m/s}$ (b) $S/D = 3$ and $u_\infty = 8\ \mathrm{m/s}$ (c) $S/D = 4$ and $u_\infty = 8\ \mathrm{m/s}$

(d) $S/D = 2.2$ and $u_\infty = 12\ \mathrm{m/s}$ (e) $S/D = 3$ and $u_\infty = 12\ \mathrm{m/s}$ (f) $S/D = 4$ and $u_\infty = 12\ \mathrm{m/s}$

(g) $S/D = 2.2$ and $u_\infty = 16\ \mathrm{m/s}$ (h) $S/D = 3$ and $u_\infty = 16\ \mathrm{m/s}$ (i) $S/D = 4$ and $u_\infty = 16\ \mathrm{m/s}$

Figure 6. Surface plots of thrust coefficient c_x.

Figure 6a, Fig. 6b and Fig. 6c can be simplified by displaying only the maximum c_x-values, as is done in Fig. 7. In these later figures, the data has been interpolated using a cubic interpolation to produce smoother surfaces, each representing the maximum thrust coefficient achievable for a given combination of speed ratios and angle of attack at a specific rotor spacing. This results in a single surface per rotor distance, effectively summarizing the optimal thrust performance across the tested parameter space. The colour gradient in Fig. 7a, Fig. 7c and Fig. 7e indicates a trend: as the rotor spacing increases, the angle of attack that yields the maximum thrust also increases. This suggests a shift in the aerodynamic interaction between rotors, with larger spacings favouring higher angles of attack for optimal performance. Based on this, it is reasonable to limit further investigation to the data of $S/D = 4$ spacing between rotors. The side force coefficient c_y corresponding to the maximum c_x values are presented in Fig. 7b, Fig. 7d and Fig. 7f. Increasing the rotor spacings from $S/D = 2$ to $S/D = 3$, results in higher side force magnitudes. In contrast, from $S/D = 3$ to $S/D = 4$ there is no significant increase of side force. In higher speed number regimes pronounced maximum peaks are visible in Figs. 7b and 7f for rotor spacings of $S/D = 2$ and $S/D = 4$, respectively. Those isolated peaks that emerge from the otherwise relatively flat plateaus, appearing at seemingly random combinations of speed ratios, are attributed to measurement or state-setting artefacts and are therefore excluded from further interpretation. The plateau regions in the c_y surfaces occur at approximately the same speed ratios as the plateaus in the c_x distributions. The minimum side force occurs when both rotors are stationary. Another notable feature of the c_y surfaces is the pronounced reduction in side force at lower speed ratios, which is a known characteristic of Flettner rotor drag

curves. This drop in side force at lower speed ratios forms a trench that becomes more developed with increased distance.

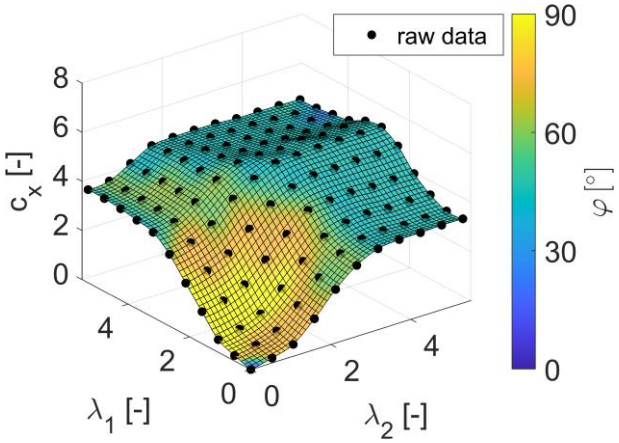

(a) Max. thrust coefficient c_x for $S/D = 2.2$ and $u_\infty = 8\ \mathrm{m/s}$

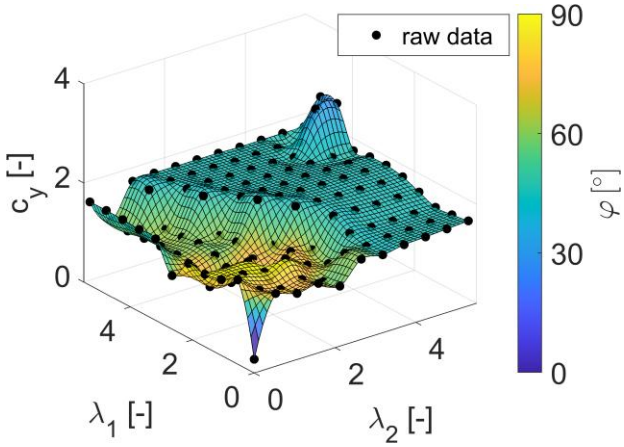

(b) Side force coefficient c_y of corresponding max. c_x for $S/D = 2.2$ and $u_\infty = 8\ \mathrm{m/s}$

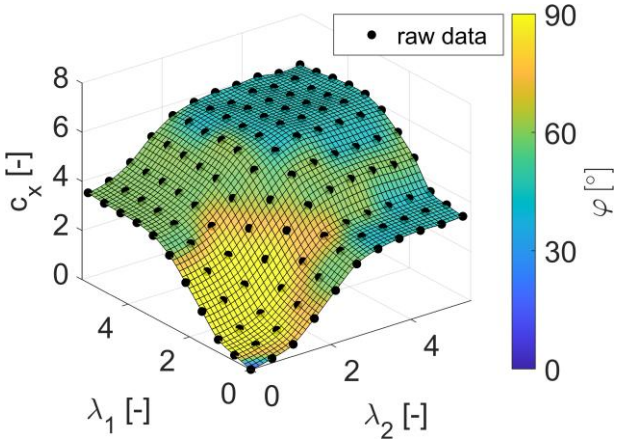

(c) Max. thrust coefficient c_x for $S/D = 3$ and $u_\infty = 8\ \mathrm{m/s}$

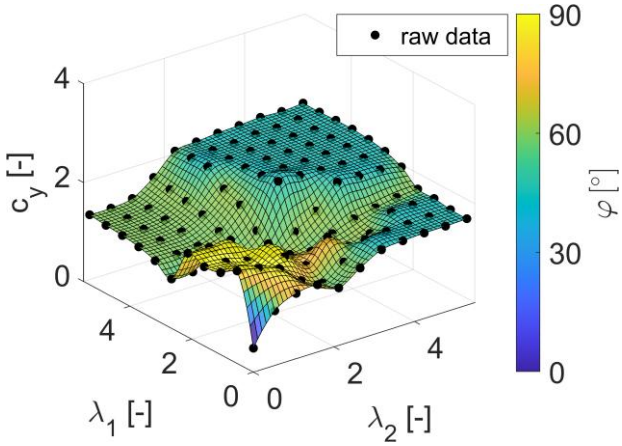

(d) Side force coefficient c_y of corresponding max. c_x for $S/D = 3$ and $u_\infty = 8\ \mathrm{m/s}$

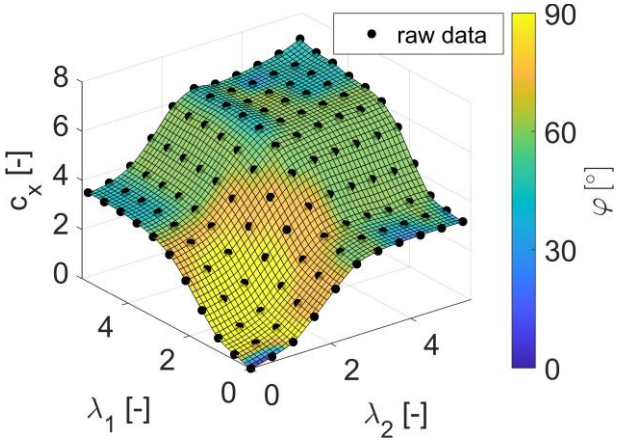

(e) Max. thrust coefficient c_x for $S/D = 4$ and $u_\infty = 8\ \mathrm{m/s}$

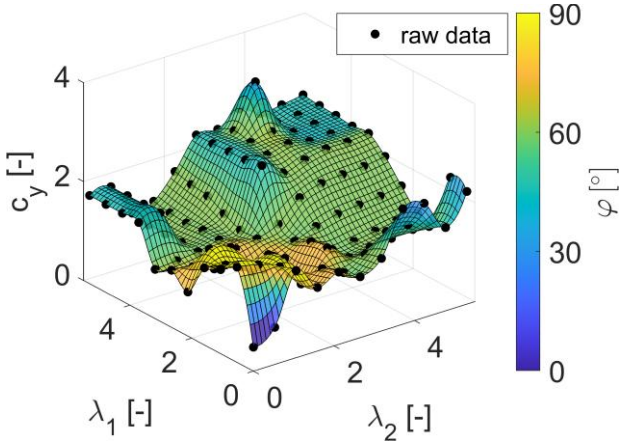

(f) Side force coefficient c_y of corresponding max. c_x for $S/D = 4$ and $u_\infty = 8\ \mathrm{m/s}$

Figure 7. Surface plots of max. thrust coefficient c_x and corresponding c_y value for all rotor spacings and $u_\infty = 8\ \mathrm{m/s}$.

The repeatability has been assessed by evaluating the range of force coefficients as difference between maximum and minimum values of each respective operating point. Between the three measurement-series repeatability was generally very good, but smaller rotor spacings S/D showed

generally larger ranges. Since only $S/D = 4$ is considered in the following, the repeatability is shown solely for this spacing. They are presented as ranges of the maximum c_x raw data points seen in Fig. 7e, with detailed values listed in Tab. 2.

Table 2. Range of c_x between three measurement series.

λ_1 \ λ_2	0	0.5	1	1.5	2	2.5	3	3.5	4	4.5	5
0	0	0.139	0.078	0.077	0.125	0.070	0.077	0.006	0.044	0.041	0.041
0.5	0.078	0.103	0.105	0.088	0.141	0.099	0.009	0.045	0.021	0.042	0.067
1	0.054	0.114	0.118	0.138	0.124	0.126	0.025	0.067	0.057	0.049	0.081
1.5	0.113	0.162	0.160	0.164	0.142	0.179	0.087	0.047	0.039	0.070	0.113
2	0.054	0.093	0.122	0.116	0.163	0.124	0.077	0.124	0.076	0.062	0.070
2.5	0.111	0.096	0.136	0.148	0.160	0.155	0.123	0.164	0.182	0.093	0.039
3	0.035	0.050	0.076	0.078	0.182	0.057	0.111	0.117	0.184	0.089	0.152
3.5	0.029	0.008	0.065	0.060	0.232	0.037	0.125	0.117	0.050	0.194	0.188
4	0.027	0.024	0.081	0.074	0.157	0.144	0.178	0.169	0.160	0.219	0.262
4.5	0.036	0.015	0.040	0.105	0.214	0.183	0.127	0.070	0.124	0.166	0.245
5	0.044	0.079	0.067	0.096	0.169	0.117	0.218	0.145	0.105	0.054	0.082

4.2 Polar Curves

The experimental setup only allows angles of attack of up to 90°, but by using the problems symmetry and changing the rotational direction, it is possible to measure the 0° to 180° data. As previously established, the wind speed has no impact on the dimensionless coefficients, so it will be exempt from evaluation. The polar curves are then defined by Eq. 16.

$$P_{c_x} = f(\lambda_1, \lambda_2, S/D, \varphi) = \begin{cases} c_{x,0-90}(\lambda_1, \lambda_2, S/D, \varphi, \alpha_c) \\ c_{x,90-180}(\lambda_1, \lambda_2, S/D, \varphi, \alpha_{cc}) \end{cases} \tag{16}$$

With α_c indicating the rotational direction as being clockwise and α_{cc} counter-clockwise. Since there are 11 tested speed ratios for both rotors, this results in 11 polar plots containing 11 curves for all speed ratio combinations. This could be repeated for the three tested distances between rotors $S/D = \{2.2, 3, 4\}$, but was deemed to result in too many figures. Later, these 11 polar plots will be combined into a singular plot, which will then be shown for the different distances as well.

In the plots shown below the radial axis gives the function values, in this case c_x, and the azimuthal axis gives the wind angle relative to the travel direction. The resulting curves are shown in Figs. 8a to 8k. It can be seen that up to 30° wind angle, almost only negative thrust is achieved for almost all speed ratio combinations. Between 30° and 45°, the thrust becomes positive and increases steadily with increasing wind angle. The maximum thrust is expected at 90°, but not achieved until 135°.

These polar curves do not contain any transformation for the apparent wind angle, as they are meant to classify the isolated double rotor system. This is intended, as now this data can be incorporated into a performance prediction process of designing a ship. The designer can transform the curves himself by adjusting the angle according to the vector triangle of true wind, vessel speed and apparent wind. Another application that emerged during the course of this research project would be a digital twin used to control the dual rotor system during operation.

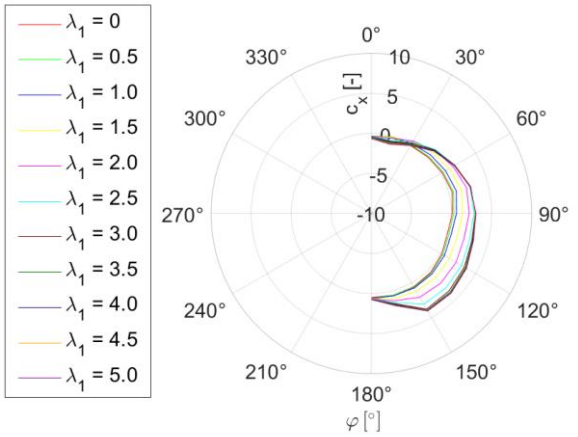

(a) c_x Polar diagram for all λ_1 and $\lambda_2 = 0$

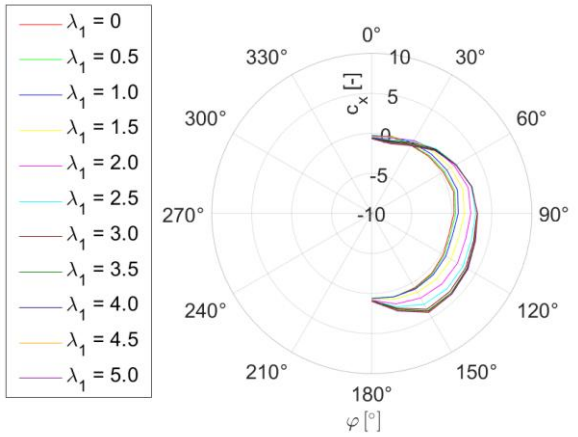

(b) c_x Polar diagram for all λ_1 and $\lambda_2 = 0.5$

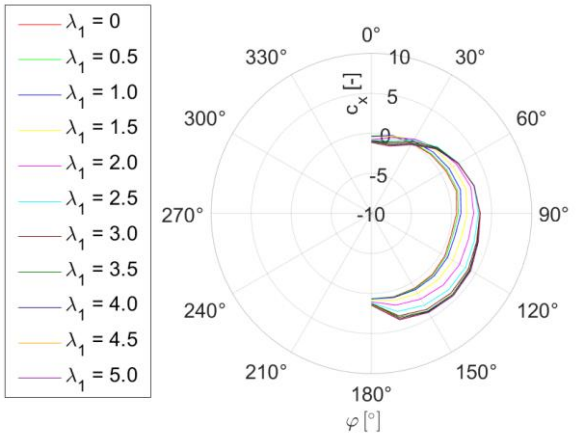

(c) c_x Polar diagram for all λ_1 and $\lambda_2 = 1$

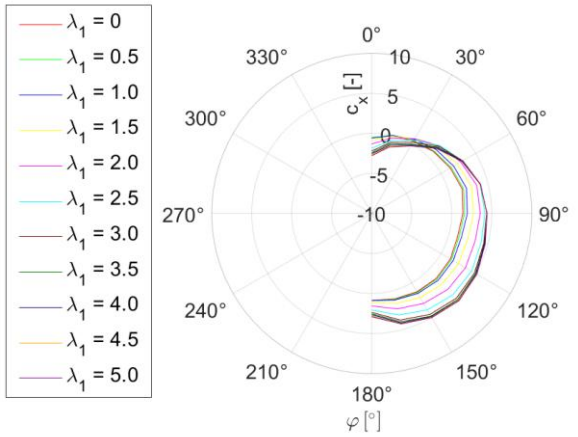

(d) c_x Polar diagram for all λ_1 and $\lambda_2 = 1.5$

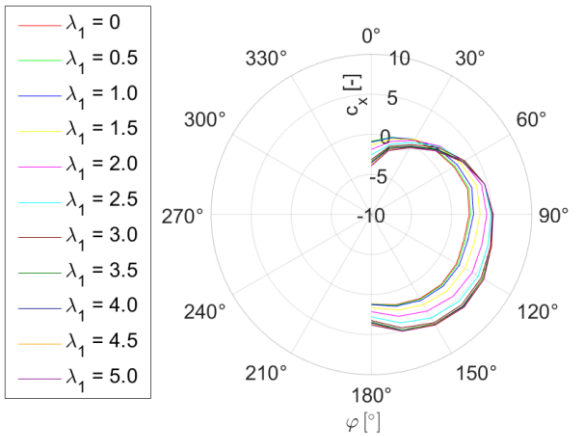

(e) c_x Polar diagram for all λ_1 and $\lambda_2 = 2$

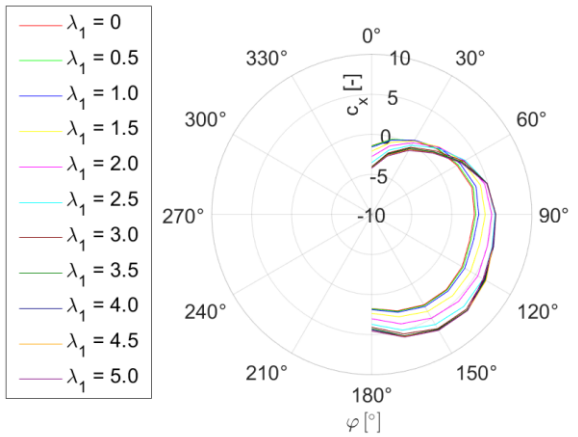

(f) c_x Polar diagram for all λ_1 and $\lambda_2 = 2.5$

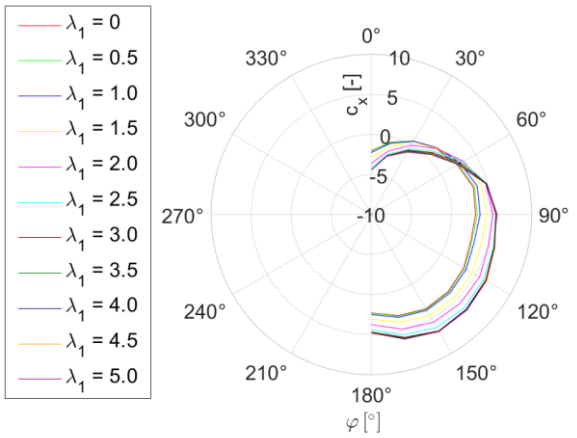

(g) c_x Polar diagram for all λ_1 and $\lambda_2 = 3$

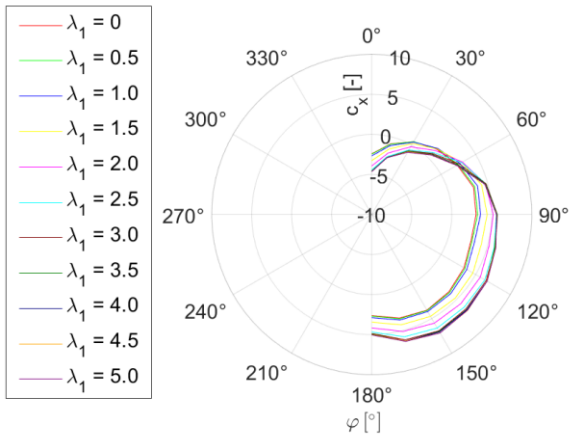

(h) c_x Polar diagram for all λ_1 and $\lambda_2 = 3.5$

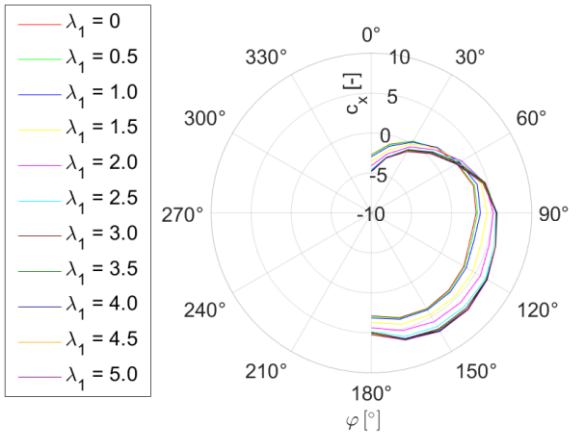

(i) c_x Polar diagram for all λ_1 and $\lambda_2 = 4$

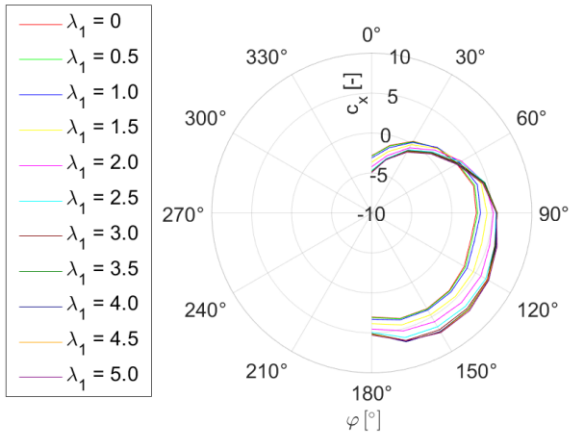

(j) c_x Polar diagram for all λ_1 and $\lambda_2 = 4.5$

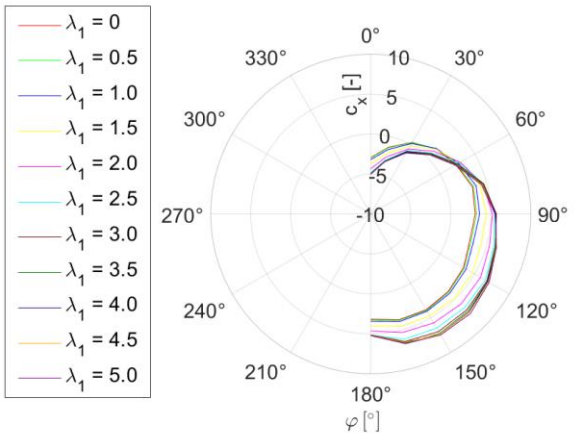

(k) c_x Polar diagram for all λ_1 and $\lambda_2 = 5$

Figure 8. c_x Polar diagrams for rotor spacing $S/D = 4$, $u_\infty = 8\,\mathrm{m/s}$ and all combinations of λ_1 and λ_2.

Compiling the maximum c_x-values out of all polar curves gives the optimal operational speed ratio for every wind direction, for a configuration where the Flettner rotors are aligned with the ship's longitudinal axis, which can be seen in Figs. 9 to 11. This kind of Flettner configuration on a ship can be called "Anton Flettner"-configuration, as Anton Flettner built the first Flettner rotor ship, the "Buckau", like this. Additionally, the polar diagrams contain the side force coefficient relating to the

respective maximum c_x-value. Figure 9 shows the polar diagram for the closest distance between rotors and Fig. 11 shows the polar diagram for the furthest distance between rotors.

Interestingly, one takeaway from Figs. 9 to 11 is that there is a relation between the distance between rotors and optimal spin ratio. The closer the rotors, the lower the optimal spin ratio. In general, the thrust values increase with greater spacing between the rotors. The flow around a rotating Flettner rotor can be imagined as a column of circulating fluid whose intensity decays with distance from the surface. The distance beyond which viscous momentum transfer ceases could be defined as the influence radius. When rotors are placed too close together, their influence radii overlap, limiting the available fluid to sustain the Magnus effect at higher spin ratios. Arising from that, the circulations interact and effectively “pull” on each other’s flow fields, shifting the attachment and detachment points, which ideally coincide at the pressure side of each rotor. For further investigation into this hypothesis a high-fidelity numerical simulation of a double rotor system for selected operating values could provide information.

It can be seen that for all distances between rotors, in the wind sector of 0° to 75°, it is not optimal to let the rotors rotate at maximum rotational speed. Only at the largest distance, the operational speed ratios for the largest c_x-values from 90° to 165° is given at $\lambda_1 = 5$ and $\lambda_2 = 5$. This supports the previously mentioned hypothesis of the influence radius of the rotors and the resulting interaction between rotors. Generally, the second rotor has its optimal operation point at larger speed ratios than the first rotor for the smaller distances. This indicates that the second rotor, due to the previously mentioned interaction of turbulence and the Magnus effect, has a more dominant Magnus effect acting on it and because of that, has a larger influence radius, impacting the first rotor negatively.

The polar curves also show that the resistance in the 0° to 30° wind sector is lower for smaller distances. This is easily explained by the lower wind speeds in the slip stream of the first rotor. At larger distances, the slip stream has more distance to recover and a higher wind speed, and thus a larger aerodynamic force, is acting on the second rotor. Also, at the closest distance, the minimal aerodynamic resistance at 0° wind angle is achieved with the second rotor turning slowly at $\lambda_2 = 1$ while the first rotor stays stationary. Similarly, at the largest distance, the same situation occurs but for $\lambda_2 = 0.5$. Only at the distance of $S/D = 3$ was the lowest resistance measured at both rotors turning slowly with $\lambda_1 = 0.5$ and $\lambda_2 = 1$. In the same way, the second rotors speed ratio is generally higher than the first rotors, which can be explained by the more turbulent inflow on the second rotor. At lower distances, the thrust generated by the Flettner rotors is overall less than at the highest distance. In addition, the first positive thrust, although very small, is already achieved at 15° wind angle. The thrust is steadily increasing from 15° to 90° for the smaller distances and from 30° to 90° for the largest distance. From 90° to 150°, the thrust keeps increasing until it decreases again from 165° to 180°.

The side forces in the “Anton Flettner”-configuration are lower than the thrust forces for smaller distances between the rotors and for wind angles of 0° to 75°. From 90° onwards the side forces become larger than the thrust forces for smaller distances between the rotors. For the larger distances, the side forces succeed the thrust forces only for the inflow angles of 105° and 120°. This concludes that not only for maximum thrust, but also for a better thrust to side force ratio, a larger distance between the rotors is more beneficial.

This polar diagram of sailing-force coefficients contains all necessary information to evaluate the systems performance, similar to that of a torque curve of an engine.

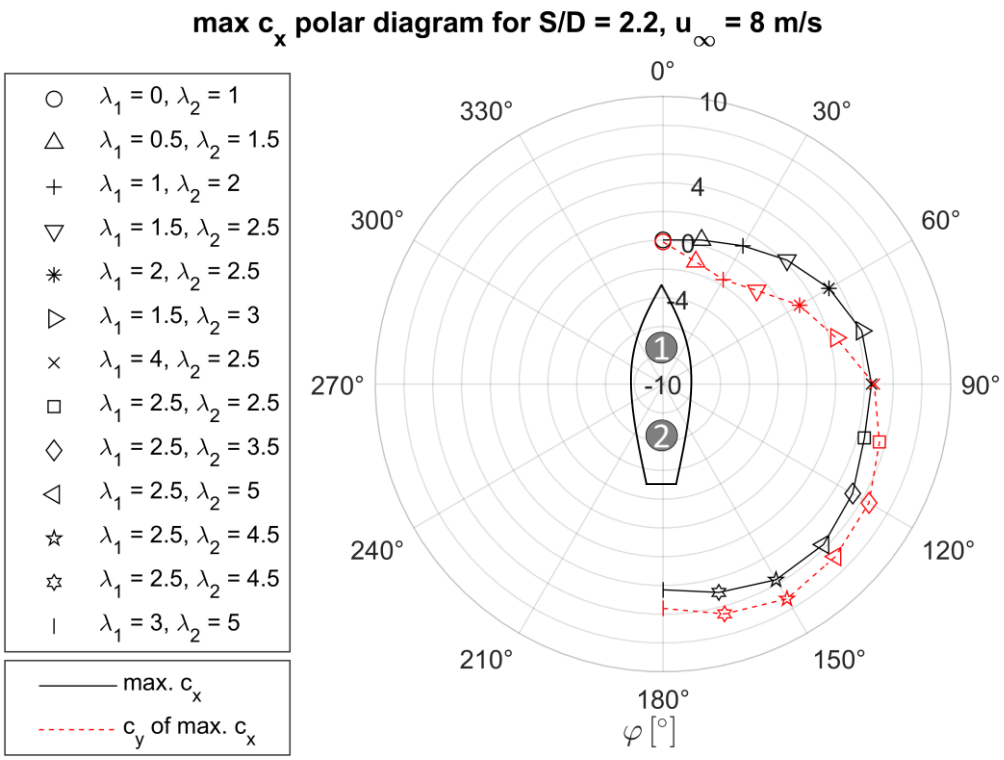

Figure 9. c_x and c_y Polar diagram for $S/D = 2.2$ and optimal λ_1 and λ_2 combinations for the "Anton-Flettner"-configuration.

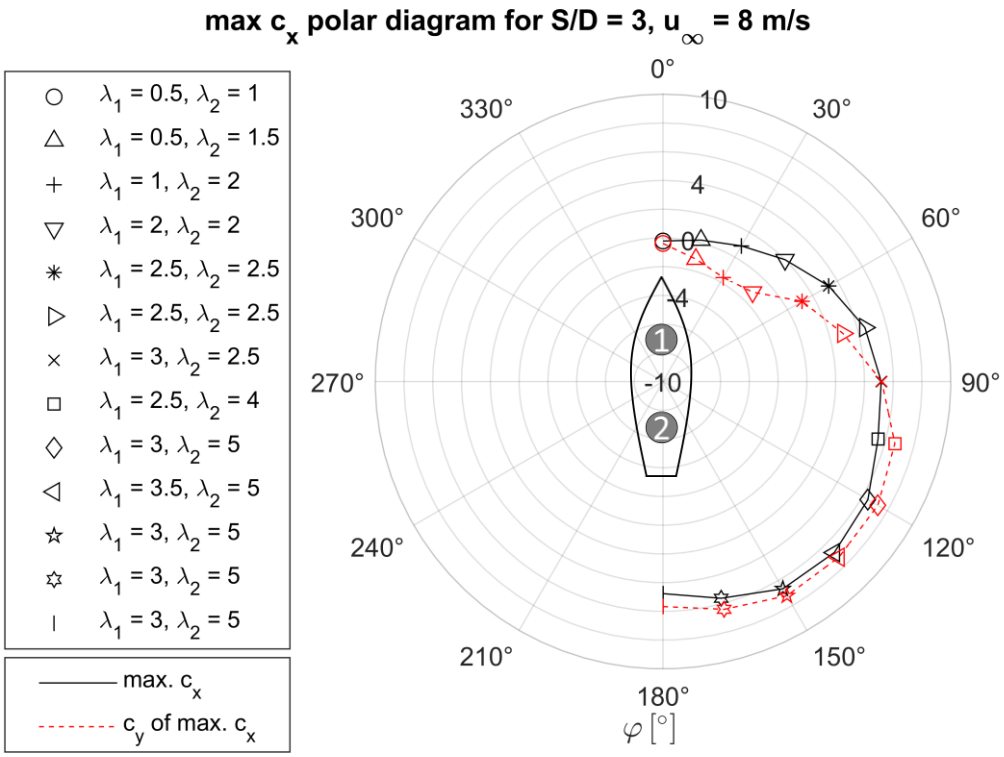

Figure 10. c_x and c_y Polar diagram for $S/D = 3$ and optimal λ_1 and λ_2 combinations for the "Anton-Flettner"-configuration.

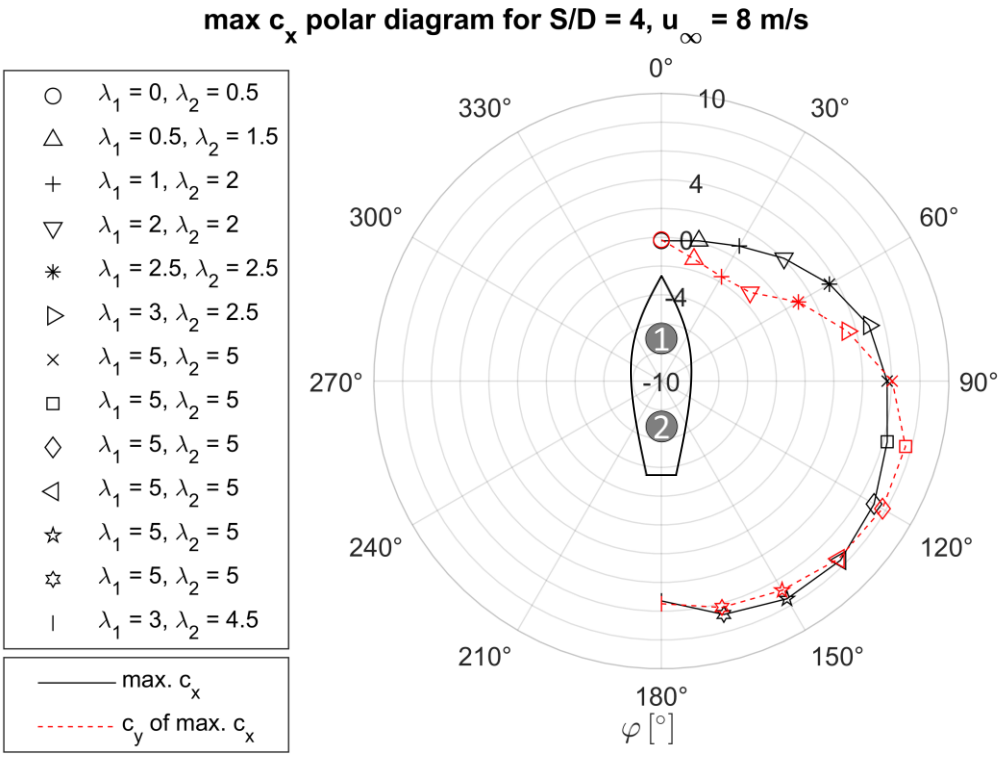

Figure 11. c_x and c_y Polar diagram for $S/D = 4$ and optimal λ_1 and λ_2 combinations for the "Anton-Flettner"-configuration.

The polar curves previously shown are only valid for a ship that is using Flettner rotors in an "Anton Flettner"-configuration. As already mentioned, it is also possible to transform the data into an assembly where the Flettner rotors are aligned with the longitudinal axis of the ship. For that purpose, simply the X- and Y-axis can be exchanged. This configuration can be called the "E-Ship1"-configuration and can be seen in Figs. 12 to 14. In comparison to the "Anton-Flettner"-configuration, the "E-Ship1"-configuration generally has higher resistance in the 0° to 30° wind sector but also smaller side forces. The total maximum thrust achieved is roughly 10% higher, $c_{x,max} = 7.47$ for the "Anton Flettner"-configuration compared to $c_{x,max} = 8.22$ for the "E-Ship1"-configuration. From 45° onwards, the thrust is steadily increasing with the inflow angle up to 165°. Similar to the "Anton Flettner"-configuration, the 90° to 180° wind sector gives the best thrust. Also, the relation between rotor spacing and thrust is the same for the "E-Ship1"-configuration, although not as pronounced.

In this configuration it is beneficial to let both rotors rotate slowly when the wind is coming from 0°, to reduce the resistance by utilizing the characteristic decrease in drag force at lower speed ratios. Although for the distance $S/D = 2.2$ the optimal operation point was measured at $\lambda_1 = 1$ and $\lambda_2 = 0$, the data points measured at $\lambda_2 = 0.5$ and $\lambda_2 = 1$ just differ slightly in the 3rd decimal. The optimal speed ratios are very different compared to the "Anton-Flettner"-configuration. More often than not, the optimal operation point is achieved with the second rotor rotating slower than the first. This supports the hypothesis of turbulence positively impacting the Magnus effect.

Based on a qualitative assessment of the energy requirements inferred from the rotor speed ratios, this configuration appears to generate greater thrust while requiring less energy than the rotors in the "Anton Flettner"-configuration. Moreover, for the smaller distances between rotors, the thrust to side force ratio is larger, meaning there will be less drifting and course deviation during travel. For the largest distance between rotors the thrust to side force ratio becomes roughly 1 in the wind sector of 105° to 120° but stays larger than 1 for all other angles.

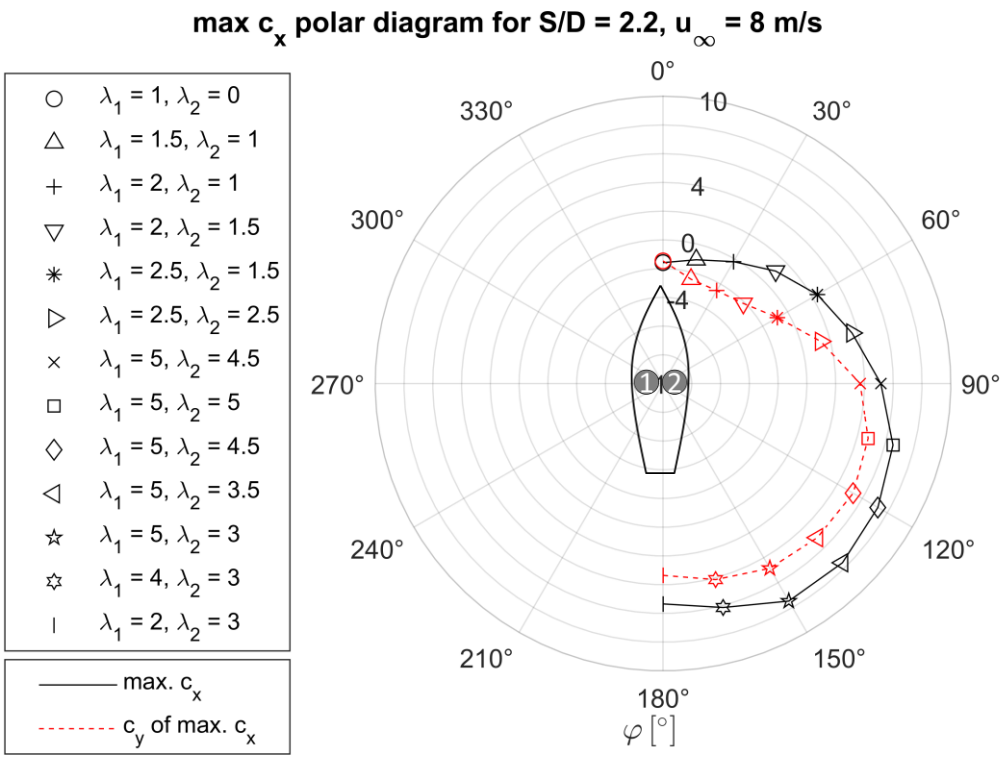

Figure 12. c_x and c_y Polar diagram for $S/D = 2.2$ and optimal λ_1 and λ_2 combinations for the "E-Ship1"-configuration.

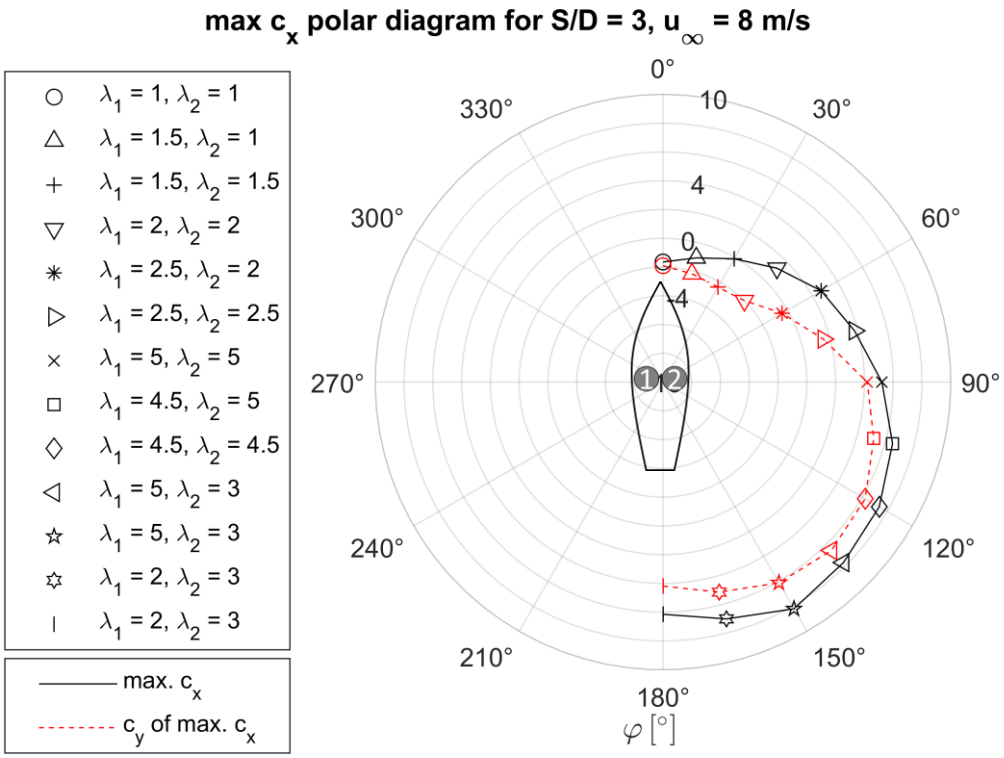

Figure 13. c_x and c_y Polar diagram for $S/D = 3$ and optimal λ_1 and λ_2 combinations for the "E-Ship1"-configuration.

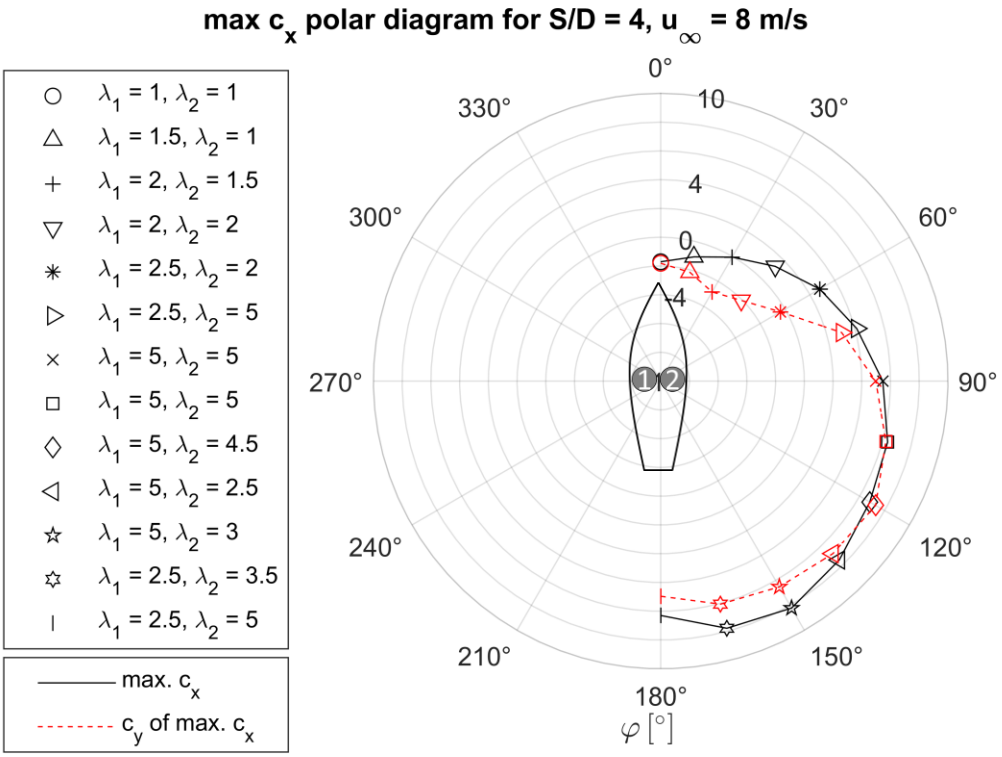

Figure 14. c_x and c_y Polar diagram for $S/D = 4$ and optimal λ_1 and λ_2 combinations for the "E-Ship1"-configuration.

5. DISCUSSION AND CONTEXT TO HISTORICAL DATA

During this investigation of the Flettner rotor in its single rotor and double rotor design, the authors were constantly questioning their own results. The same Flettner rotor model was used in two different wind tunnels, the wind tunnel of Emden/Leer University in its Eiffel design and in a larger wind tunnel of another unnamed institution that was constructed after the Göttingen design. First, the difference in results between those measurement series was said to be the force sensors, since all the other operational variables were kept the same. But even then, the difference of 30% between results of the lift value was deemed too much. Intensive literature research has been done to compare not only our results but also our methodology to state of the art and historical research. The result can be seen in Fig. 15, where only lift values that make sense in the context of this discussion are shown. In short, only research that investigated speed ratios up to a value of $\lambda = 4$ was taken into account while keeping rotor dimensions and Reynolds number in mind, but not used as excluding parameters. The data recorded with the Flettner rotor model of Emden/Leer University are shown as thick red and black lines, red being for the data from the Göttingen wind tunnel and black being from the Eiffel wind tunnel. The black lines maximum lift value is $c_L = 7.2$ at speed ratio $\lambda = 5$, while the red lines maximum lift value is $c_L = 10.67$ at speed ratio $\lambda = 5$. The differences were also present in the drag values, but not as pronounced and in opposite manner.

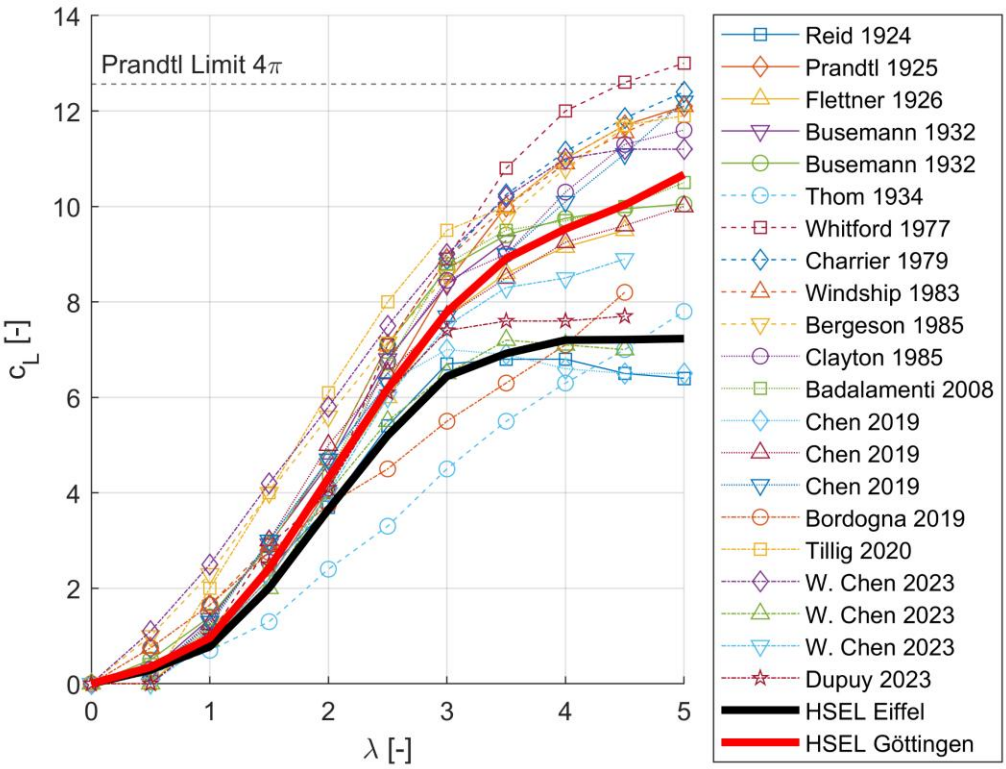

Figure 15. Lift values for single Flettner rotors found in academic literature.

Starting with the data of Reid (1924), that used a cylinder of 0.1143 m diameter and "tested in infinite length-diameter ratio", meaning that the cylinder started and ended with the wind tunnels boundaries, translating into an infinite aspect ratio and infinite endplate ratio. Reid reported a maximum lift value of $c_L = 9.5$ at a wind speed of $u_\infty = 5\ \mathrm{m/s}$ and a speed ratio of $\lambda = 4.3$. Later, Prandtl (1925) reported on his experiments with rotating cylinders and found that lift values drastically increase when plates are added to the ends of the cylinder. He achieved a maximum lift value of $c_L = 9.3$ and derived the theoretical limit of a rotating cylinder at $c_L = 4\pi$ using potential theory on the problem of a 2D rotating cylinder. The cylinder used in these experiments had a diameter of 0.07 m, a length of 0.33 m and endplates of 0.145 m diameter. During this time, Anton Flettner built the first rotor ship, the "Buckau", and reported on its rotor's performance to be $c_L = 10$ measured on rotors of 3 m diameter and 15 m in height Flettner (1926). Complementary to this, Busemann (1932) did more experiments on cylinders of 0.06 m diameter, 0.101 m and 0.72 m of length and different endplate diameters. In this context, only results for rotors with endplates of $D_e/D = 2$ were taken into consideration. The short cylinder achieved a lift value of $c_L = 6.4$ while the lift of the longer cylinder was measured at $c_L = 12$. Another publication from the same time frame was written by Thom (1934) who reported a lift value of $c_L = 8$ for speed ratio of $\lambda = 5$. His rotor was of dimensions 0.0508 m in diameter and 0.635 m in length and used endplates with a ratio of $D_e/D = 3$.

From this historical research data, it was considered that in the Emden/Leer University Eiffel wind tunnel some early flow separation was taking place and that the Magnus effect was not acting on the full length of the rotor, thus achieving lower lift values. For validating this hypothesis, a pitot tube anemometer was used to sample the flow close to the rotor surface over the whole length of the rotor. Surprisingly, the flow velocity was similar for all probed points along the rotor length, disproving the hypothesis.

Other results like those from Whitford, et al. (1978) suggested that even higher lift values were possible. Their wind tunnel experiments on a rotor with 0.025 m diameter and 0.152 m length measured lift values of $c_L = 13$ for endplates of ratio $D_e/D = 2$ and $c_L = 14$ for $D_e/D = 3$ endplates.

This challenges the idea of the previously mentioned Prandtl limit. Another investigation by Charrier (1979) reported a lift value of $c_L = 12.4$ at speed ratio $\lambda = 5$ on a rotor with aspect ratio of 5. Bergeson and Greenwald (1985) did measurements on a Flettner rotor on a small ship. The rotors dimensions were 1.16 m in diameter and 7.22 m in height. Similarly, they stated that the lift value $c_L = 12$ is achieved at speed ratio of $\lambda = 5$. In line with that, Clayton (1985) reported a lift value of $c_L = 11.5$ at speed ratio $\lambda = 5$ on a rotor with aspect ratio of 8. Noticeably, not all parameters of the tested objects can be found in the papers from this era of Flettner rotor research. This gave reason to think that compared to our measurements, the large differences in lift values could be a result of different Reynolds numbers or rotor dimensions. One more suspicion was that the skin friction of the 3D printed Flettner rotors tested at Emden/Leer University was different from the tested rotors from literature. This was immediately dismissed, as the old model tested previously in both wind tunnels was made from aluminum.

Newer results from Badalamenti and Prince (2008) achieved a lift value of $c_L = 10.5$ at speed ratio $\lambda = 5$ and $D_e/D = 2$ endplates. Chen and Rheem (2019) investigated rotating cylinders with small aspect ratios and 0.6 m length. For an aspect ratio of 1.85, meaning the rotor was 0.319 m in diameter, a lift value of $c_L = 6.5$ was reported. The rotors with larger aspect ratios (2.21 and 2.73) achieved much higher lift values of $c_L = 10$ and respectively $c_L = 12.2$. For the rotor with aspect ratio of 2.73 they even reported a lift value of $c_L = 13$ at $\lambda = 5.4$, but commented that this does not support to conclude that the Prandtl limit can be exceeded. No further reasoning was given on why, but it is assumed that experiment's accuracy is in the range of deviation from the Prandtl limit. Studies by Bordogna, et al. (2019) explored a Reynolds number dependency of Flettner rotors in the speed ratio region of $1 < \lambda \leq 2.5$ and reported an "overall"-lift value of $c_L = 8.2$ at speed ratio $\lambda = 4.5$ for a rotor of 1 m diameter and 3.73 m height. This gave reason to think that either our results were not too far off, or Bordogna had the same systematic experiment artifact in his data, that affected the single rotor results from Emden/Leer Universities Eiffel wind tunnel. Since this was the first result suggesting this, it felt handpicked and more data from literature was gathered for comparison. A publication by Tillig and Ringsberg (2020) showed a set of data from measurements on a real ship with a 4 m diameter by 24 m height Flettner rotor installed. The lift value measured at $\lambda = 5$ is at $c_L = 11.9$ and the inconsistency to Bordogna's data was explained with scale effects and the Reynolds number dependency. Close to this present study, Chen, et al. (2023) also investigated a double Flettner rotor system. Before focusing on the double rotor layout, geometry variations of a single rotor were investigated. The lift values at $\lambda = 4.5$ displayed by Chen were $c_L = 7$ for Reynolds number $Re = 9.33 \times 10^4$ and $c_L = 8.9$ for Reynolds number $Re = 3.15 \times 10^5$ on a rotor that is 0.35 m in diameter, 2.1 m in height and has a $D_e/D = 1.6$ endplate ratio. These results are in line with measurements at the Emden/Leer University facility and with the data presented by Bordogna. Therefore, it was thought that measurement devices and experimental setups have increased in accuracy by a lot between 1924 and 2025 and that is where the problem is rooted. This still did not explain the difference between Emden/Leer Universitie's own results, measured in two different wind tunnels of different construction type. Additionally, Dupuy, et al. (2023) reported a lift value of $c_L = 11.2$ for a 35 m high rotor with a diameter of 5 m, measured during ship operation at $\lambda = 5$. It is striking, that all of the real size rotor measurements are at the upper end of the variance in the results while the more recent results are more in line with each other at the lower end of the data variance. In accordance with this, Vahs (2020) also reported a difference of up to 20% between force values prognosed by model experiments and measured in test trials of the real size Flettner rotor.

Not until the final stages of the double rotor system investigation, an explanation for this deviation was found finally. As the data was being evaluated, not only the total forces exerted by the whole system, but also the individual forces of the two rotors were looked at. In the course of this individual rotor investigation, an anomaly was found as seen in Fig. 16. Rotor 2 is the first rotor hit by the wind and at 0°, 60° and 75° the lift-curves are almost the same. On the other hand, rotor 1 is standing in the wake of rotor 2 and it would be expected that, equivalent to the wake effect on wind turbines, its performance would be less. Conversely to that assumption, it was found that the rotor standing in the wake had an increased performance. In addition to that, at 90° where both rotors are hit by undisturbed wind, the lowest performance is found.

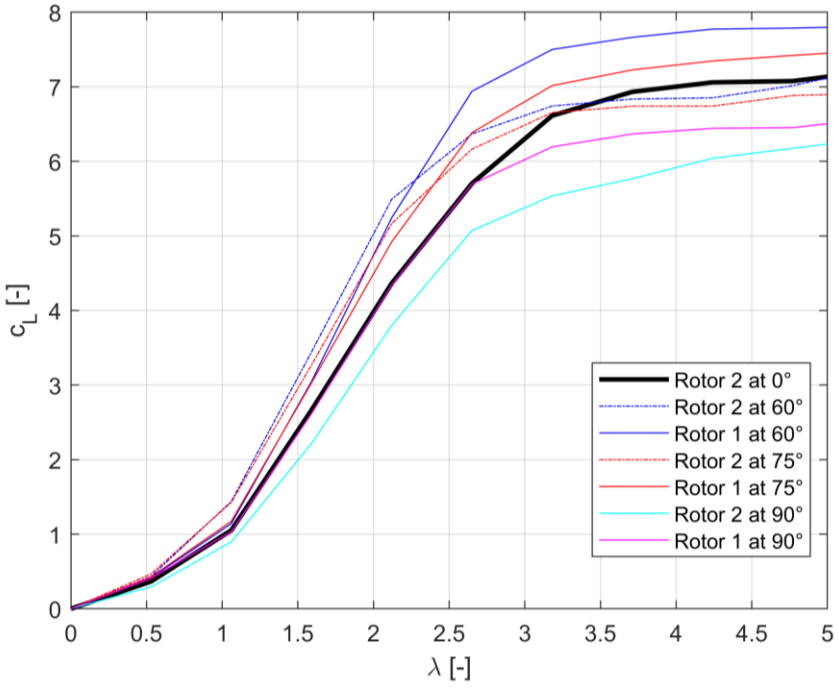

Figure 16. Lift values for individual Flettner rotors in the double rotor experiment at different angles of attack at distance $S/D = 4$.

It has been shown that there is a huge variance in publicized data for Flettner rotors and that even when the same model is investigated in two different facilities, a huge difference can occur. No satisfying explanation was found by the comparison of data and methodology. From investigation of forces measured at individual rotors in a double rotor experiment, it was seen that there is an unusual increase in the lift force on the rotor standing in the wake. For the double rotor experiments presented in this study, the conditions of the inflow are exceptionally controlled and laminar. The wind tunnel used is the WK 880050-E which has a turbulence intensity of 0.5% to 0.8% at 20 m/s wind speed, accredited by the national German Accreditation Office. The experiments were mostly done at 8 m/s wind speed, with a turbulence intensity of 0.8% or lower as inflow condition on rotor 2, which is the first rotor hit by the wind. For the inflow on rotor 1 (downstream), this does not hold anymore, because the inflow is modified by the rotor 2 (upstream) already, so it is expected to have a different local mean velocity and local inflow angle as well as increased local turbulence intensity. At fixed rotor speeds, the effective speed ratio therefore changes with changing local wind speed. A change in the effective speed ratio has the consequence of a change in the measured lift force. If the local mean wind speed decreases, as in a normal wake effect, the effective speed ratio at the downstream rotor increases and the lift force increases until saturation. If the local wind speed at the downstream rotor increases through momentum transfer from the upstream rotors' rotation into the fluid, the measured lift force will increase. The change in the lift coefficient will be unrecognizable in the case of decreasing wind speed, as the force only experiences minor changes in magnitude and the normalization is done with the free stream wind speed and not the local wind speed. In the case of an increase in local wind speed, the change in lift force is large enough to be recognized in the lift coefficient, because of said normalization. Concluding from that, Flettner rotors, or rotating cylinders, have a different relation to mean velocity wake effects than rigid objects or wind turbines. Whether the local wind speed in the wake of a Flettner rotor will decrease or increase will be investigated in a follow-up measurement campaign. From other aerodynamic experiments with stationary and rigid profiles it is known that a more laminar inflow is more beneficial for the measured forces. The measured forces suggest that not only the mean wind speed but also the wind speeds fluctuations (turbulence) have an impact on the Magnus effect. Physically one can plausibly interpret this by exploring the relation between turbulence intensity and the kinetic energy of the turbulent fluid, which can be seen in Eq. 10. The kinetic energy increases quadratically with turbulence intensity. Turbulent kinetic energy k characterizes the intensity of velocity fluctuations. Together with a comparable

dissipation rate ε, it increases the turbulent eddy viscosity, as seen in Eq. 12 and thus improves turbulent mixing. This shifts boundary layer attachment and detachment points on the cylinder. Elevated k promotes earlier transition and more robust attachment on the advancing side, while delaying detachment, increasing the resulting Magnus force. This makes the turbulence intensity an indispensable information for the evaluation of data on the Magnus effect. This wake effect was also recently investigated numerically by Zhang, et al. (2024), who found an increase of 23% through utilization of wake energy. In accordance with this, the laminar flow field of double Flettner rotor experiments becomes critical, because without it this beneficial effect would not be measurable. As already mentioned earlier, an investigation of turbulence effects on Flettner rotors and how to practically utilize them is in progress and will be published soon.

6. CONCLUSIONS

In this study, an extensive series of wind tunnel experiments was conducted on a double Flettner rotor system, systematically varying six key parameters: Rotational speed of both rotors, angle of attack, distance between rotors, wind speed and rotational direction, resulting in a total of 10164 individual measurements. The experiment with such a large parameter space was made possible through a fully automated experimental setup, enabling the setting of parameters during wind tunnel operation, repeated three times for validation, showing excellent repeatability.

Furthermore, a data reduction strategy was outlined, that allows the visualization of this large dataset in just a few important plots. It was shown that the overall performance of the double rotor system can be effectively characterized using a two-line plot of the thrust- and side force coefficients c_x and c_y across operating conditions. This representation offers a clear and intuitive means of assessing rotor performance, analogous to the torque curve of an internal combustion engine.

The data gives an overview of how the parameters λ_1, λ_2, S/D and φ jointly impact the thrust coefficient of a double rotor system within the defined parameter space. For the tested rotor spacings of $S/D = \{2.2, 3, 4\}$ it was shown that increasing rotor spacing generally increased the thrust. Rotor spacings beyond $S/D = 4$ could not be tested, because the experimental setup did not allow larger spacings. The existence of asymmetric spin pairs was shown for the double rotor system, where the leeward rotor is rotating up to 50% faster than the windward rotor. The reason for that has been identified as wake interactions, where at an angle of $\varphi = 60°$ an up to 11% increased lift force was measured at the rotor standing in the wake compared to the rotor in undisturbed flow. The wake interaction has been acknowledged and will be investigated in depth and published in a follow-up paper. Different arrangements on deck of a vessel have been evaluated, showing that an arrangement of Flettner rotors along the lateral axis of the vessel generates 10% higher thrust values when comparing the maximum achieved thrust for all wind angles.

Beyond the experimental campaign itself, this work critically examined the definition of the Reynolds number for rotating cylinders and its implications for comparing published data. A large collection of published data was used to compare to this study's results. The observed variance in prior results was attributed primarily to differences in Reynolds number and turbulence intensity. By separately analyzing the upstream and downstream rotors, the study demonstrated a positive influence of turbulence on the Magnus effect, providing further insight into the aerodynamic behavior of interacting rotors.

The dataset will be implemented in the backend of several applications currently in development: a manoeuvring simulation for vessels equipped with Flettner rotors, a deck-layout design optimizer for rotor placement, and a digital twin that ingests real-time on-board wind measurements to recommend optimal control settings. All applications will utilize look-up tables giving c_x and c_y of individual rotors for all possible combinations of λ_1, λ_2, S/D and φ. To illustrate how the measured coefficients can be applied for performance prediction in practice, consider the following example scenario.

The measured lookup table for c_x and c_y can be applied to a specific operating scenario to estimate forces in physical units. Consider a model vessel equipped with two rotors ($D = 3\,\mathrm{m},\ L = 18\,\mathrm{m}$, reference area of the double rotor system $A = 2LD$), spaced at $S/D = 4$ and aligned laterally. For this example, the inflow angle is $\varphi = 150°$ and the wind speed is $u_\infty = 8\,\mathrm{m/s}$ at air density $\rho = 1.225\,\mathrm{kg/m^3}$. From the derived polar curves (Eq. 16) we get for equal spin ratios:

$$P_{c_x}\,(\lambda_1 = 5, \lambda_2 = 5, S/D = 4, \varphi = 150°) = 7.75$$
$$P_{c_y}\,(\lambda_1 = 5, \lambda_2 = 5, S/D = 4, \varphi = 150°) = 7.08$$

And for asymmetric spin ratios:

$$P_{c_x}\,(\lambda_1 = 5, \lambda_2 = 3, S/D = 4, \varphi = 150°) = 8.22$$
$$P_{c_y}\,(\lambda_1 = 5, \lambda_2 = 3, S/D = 4, \varphi = 150°) = 6.52$$

The projected thrust force is calculated according to a rearranged Eq. 4. For the equal spin ratio pair, the thrust and side force is then

$$F_x = c_x 0.5 \rho A u_\infty^2 = 7.75 \times 0.5 \times 1.225\,\mathrm{kg/m^3} \times 2 \times 18\,\mathrm{m} \times 3\,\mathrm{m} \times 8^2\,\mathrm{m^2/s^2} = 32810\,\mathrm{N}$$
$$F_y = c_y 0.5 \rho A u_\infty^2 = 7.08 \times 0.5 \times 1.225\,\mathrm{kg/m^3} \times 2 \times 18\,\mathrm{m} \times 3\,\mathrm{m} \times 8^2\,\mathrm{m^2/s^2} = 29974\,\mathrm{N}$$

And for the asymmetric spin ratio pair, the thrust and side force

$$F_x = c_x 0.5 \rho A u_\infty^2 = 8.22 \times 0.5 \times 1.225\,\mathrm{kg/m^3} \times 2 \times 18\,\mathrm{m} \times 3\,\mathrm{m} \times 8^2\,\mathrm{m^2/s^2} = 34800\,\mathrm{N}$$
$$F_y = c_y 0.5 \rho A u_\infty^2 = 6.52 \times 0.5 \times 1.225\,\mathrm{kg/m^3} \times 2 \times 18\,\mathrm{m} \times 3\,\mathrm{m} \times 8^2\,\mathrm{m^2/s^2} = 27603\,\mathrm{N}$$

In this example the thrust force is increased by 6% and the side force is decreased by 8% by using asymmetric spin ratios instead of equal spin ratios. Such an increase in thrust combined with the reduction in side force is advantageous for route optimization and control strategies. This kind of calculation can be done in any kind of backend of any program that is interested in forces exerted by a double rotor system with the data of the polar curve function P_{c_x} and P_{c_y} provided as lookup tables. The polar curves for P_{c_x} and P_{c_y} are provided as supplementary material (see Supplementary Material, Sec. 1) for reference and reuse.

The study's experimental setup has limitations. The maximum rotor spacing investigated was $S/D = 4$, constrained by the dimensions of the wind tunnel test section. Likewise, rotor speed was capped at 10000 rpm due to the bearing specifications; however, this limit was not reached in the tests, as the highest spin ratio of $\lambda = 5$ was achieved at approximately 9000 rpm. Also, it has to be noted that the observed wake mechanism was not directly measured, but merely interpreted from the measured forces. A detailed investigation into the turbulence sensitivity of the Magnus effect is still in progress.

ACKNOWLEDGEMENTS

This work has been funded by the German Federal Ministry of Economic Affairs and Climate Action under the Grant Agreement Number 03SX581G. We appreciate the financial support which allowed us to conduct this work and good cooperation with our partners in the FlettnerFLEET project.

REFERENCES

Achenbach, E. (1968). Distribution of Local Pressure and Skin Friction Around a Circular Cylinder in Cross-Flow up to Re = 5 × 10^6. *Journal of Fluid Mechanics.* 34. 4. pp. 625–639. DOI: 10.1017/S0022112068002120.

Badalamenti, C., and Prince, S. (2008). The Effects of Endplates on a Rotating Cylinder in Crossflow. *AIAA Applied Aerodynamics Conference.* 26.

Bergeson, L., and Greenwald, K. (1985). Sail Assist Developments 1979-1985. *Journal of Wind Engineering and Industrial Aerodynamics.* 19. pp. 45–114.

Bordogna, G., Muggiasca, S., Giappino, S., Belloli, M., Keuning, J., and Huijsmans, R.H.M. (2020). The Effects of the Aerodynamic Interaction on the Performance of two Flettner Rotors. *Journal of Wind Engineering and Industrial Aerodynamics.* 196. pp. 104024. DOI: 10.1016/j.jweia.2019.104024.

Bordogna, G., Muggiasca, S., Giappino, S., Belloli, M., Keuning, J., Huijsmans, R.H.M., and van 't Veer, A. (2019). Experiments on a Flettner Rotor at Critical and Supercritical Reynolds Numbers. *Journal of Wind Engineering and Industrial Aerodynamics.* 188. pp. 19–29. DOI: 10.1016/j.jweia.2019.02.006.

Busemann, A. (1932). Messungen an Rotierenden Zylindern. Ergebnisse der Aerodynamischen Versuchsanstalt zu Göttingen. 4. pp. 101–105.

B. Charrier (1979). Étude Théorique et Expérimentale de L'effet "Magnus" Destiné à la Propulsion Éolienne de Navires. Paris.

Chen, W., and Rheem, C. (2019). Experimental Investigation of Rotating Cylinders in Flow. *Journal of Marine Science and Technology.* 24. 1. pp. 111–122. DOI: 10.1007/s00773-018-0535-5.

Chen, W., Wang, H., and Liu, X. (2023). Experimental Investigation of the Aerodynamic Performance of Flettner Rotors for Marine Applications. *Ocean Engineering.* 281. pp. 115006. DOI: 10.1016/j.oceaneng.2023.115006.

Clayton, B. (1985). BWEA Initiative on Wind Assisted Ship Propulsion (WASP). *Journal of Wind Engineering and Industrial Aerodynamics.* 19. pp. 251–276.

Dupuy, M., Letournel, L., Ville, P., Rongère, F., Sarsila, S., and Vuillermoz, L. (2023). Weather Routing Benefit for Different Wind Propulsion Systems. *International Conference on Innovation in High Performance Sailing Yachts and Wind-Assisted Ships.*

A. Flettner (1926). The Story of the Rotor. New York. F.O. Willhofft.

Foiles, W., and Allaire, P. (2006). Single Plane and Multi-Plane Rotor Balancing Using Only Amplitude. *Conference: 7th IFToMM-Conference on Rotor Dynamics.*

Glauert, H. (1933). Wind Tunnel Interference on Wings, Bodies and Airscrews. *Aeronautical Research Committee Reports and Memoranda.* 1566.

Karabelas, S., Koumroglou, B., Argyropoulos, C., and Markatos, N. (2012). High Reynolds Number Turbulent Flow Past a Rotating Cylinder. *Applied Mathematical Modelling.* 36. 1. pp. 379–398. DOI: 10.1016/j.apm.2011.07.032.

Karman, T. von (1931). Mechanical Similitude and Turbulence. NACA-TM-611.

Ma, W., Liu, J., Jia, Y., Jin, L., and Ma, X. (2022). The Aerodynamic Forces and Wake Flow of a Rotating Circular Cylinder Under Various Flow Regimes. *Journal of Wind Engineering and Industrial Aerodynamics.* 224. pp. 104977. DOI: 10.1016/j.jweia.2022.104977.

Prandtl, L. (1904). Über Flüssigkeitensbewegung bei sehr Kleiner Reibung. *Verhandlungen des III. Internationalen Mathematiker-Kongresses.*

Prandtl, L. (1925). Magnuseffekt und Windkraftschiff. *The Science of Nature.* 13. 6. pp. 93–108. DOI: 10.1007/BF01585456.

Reid, E. (1924). Tests of Rotating Cylinders. NACA-TN-209.

Thom, A. (1934). Experiments on the Flow Past a Rotating Cylinder. H. M. Stationery Office.

Tillig, F., and Ringsberg, J. (2020). Design, Operation and Analysis of Wind-Assisted Cargo Ships. *Ocean Engineering.* 211. pp. 107603. DOI: 10.1016/j.oceaneng.2020.107603.

Vahs, M. (2020). Retrofitting of Flettner Rotors - Results from Sea Trials of the General Cargo Ship "Fehn Pollux". *International Journal of Maritime Engineering.* 162. A4. DOI: 10.3940/rina.2020.a4.641.

Whitford, D., Minardi, J., West, B., and Dominic, R. (1978). An Analysis of the Madaras Rotor Power Plant. 1.

Zhang, R., Huang, L., Wang, K., Ma, R., Ruan, Z., and Wang, C. (2024). Novel Optimized Layout for Flettner Rotors Based on Reuse of Wake Energy. *Journal of Cleaner Production.* 443. pp. 140922. DOI: 10.1016/j.jclepro.2024.140922.